J. Fluid Mech. (2011), *vol.* 667, *pp.* 48–84.
doi:10.1017/S0022112010004337

Boundary-layer hydrodynamics and bedload sediment transport in oscillating water tunnels

DAVID GONZALEZ-RODRIGUEZ† AND OLE SECHER MADSEN

Department of Civil and Environmental Engineering, Massachusetts Institute of Technology, Cambridge, MA 02139, USA

(Received 24 December 2009; revised 1 August 2010; accepted 11 August 2010; first published online 1 November 2010)

Oscillating water tunnels are experimental facilities commonly used in coastal engineering research. They are intended to reproduce near-bed hydrodynamic and sediment transport phenomena at a realistic scale. In an oscillating water tunnel, a piston generates an oscillatory motion that propagates almost instantaneously to the whole tunnel; consequently, flow is uniform along the tunnel, unlike the propagating wave motion in the sea or in a wave flume. This results in subtle differences between the boundary-layer hydrodynamics of an oscillating water tunnel and of a propagating wave, which may have a significant effect in the resulting sediment transport. In this paper, we present a zeroth-order analytical model of the turbulent boundary-layer hydrodynamics in an oscillating water tunnel. By using a time-varying eddy viscosity and by accounting for the constraints arising from the tunnel's geometry, the model predicts the oscillating water tunnel hydrodynamics and yields analytical expressions to compute bed shear stresses for asymmetric and skewed waves, both in the absence or presence of an imposed current. These expressions are applied to successfully quantify bedload sediment transport in oscillating water tunnel experiments.

Key words: coastal engineering, sediment transport, turbulent boundary layers

1. Introduction

Prediction of near-shore sediment transport is a central problem in coastal engineering. Near-shore waves are both asymmetric (forward-leaning in shape) and skewed (with peaked, narrow crests and wide, flat troughs). The effect of such wave shapes on sediment transport is not well understood, and it has recently been the object of extensive modelling efforts. Two very different types of approaches are found in the literature. The first mainstream approach consists of numerical simulation of hydrodynamics and fluid–sediment interactions. The effect of boundary-layer hydrodynamics on sediment transport is often investigated by numerically solving the Reynolds-averaged Navier–Stokes equations together with k–ϵ or k–ω turbulence closures (e.g. Henderson, Allen & Newberger 2004; Holmedal & Myrhaug 2006; Fuhrman, Fredsoe & Sumer 2009; Ruessink, van den Berg & van Rijn 2009). Other numerical approaches include detailed descriptions of fluid–particle interactions, using discrete particle simulations (e.g. Drake & Calantoni 2001; Calantoni & Puleo 2006),

† Present address: Institut Curie, UMR 168, 11–13 rue Pierre et Marie Curie, 75005 Paris, France. Email address for correspondence: davidgr@alum.mit.edu

as well as two-phase models (e.g. Hsu & Hanes 2004; Liu & Sato 2006). In spite of the valuable amount of detail provided, these numerical approaches are often too computationally demanding for practical applications, since sediment transport models need to be applied iteratively to account for the continuously evolving morphology of the beach profile. The second mainstream approach aims for simplicity, by proposing practical formulations for computing sediment transport. Within these we find semi-empirical or conceptual formulations (e.g. Dibajnia & Watanabe 1992; Watanabe & Sato 2004; Nielsen 2006; Silva, Temperville & Santos 2006; Gonzalez-Rodriguez & Madsen 2007; Suntoyo, Tanaka & Sana 2008), some of which involve parameters that need to be calibrated against hydrodynamic or sediment transport data. In contrast with these two mainstream procedures, this paper proposes an analytical approach to the prediction of near-shore sediment transport, which captures the underlying physical processes while retaining computational efficiency for practical application. A previous analytical study of surf zone hydrodynamics was proposed by Foster, Guenther & Holman (1999), who modelled propagating waves of arbitrary shape using a time-varying eddy viscosity model similar to that of Trowbridge & Madsen (1984*a*). Unlike Trowbridge and Madsen, Foster *et al.* neglected the effect of the nonlinear wave propagation term. Foster *et al.*'s analysis results in integral expressions for the hydrodynamic magnitudes that need to be evaluated numerically; in contrast, this paper presents explicit expressions that are readily applicable to prediction of sediment transport. It is noted that, when applying their model to quantify sediment transport, Foster *et al.* predict that purely asymmetric waves yield a net offshore sediment transport, which is in disagreement with experimental observations (King 1991; Watanabe & Sato 2004; van der A, O'Donoghue & Ribberink 2010).

Many of the experimental studies of near-shore sediment transport that are used for model validation have been conducted in oscillating water tunnels, a type of facility that attempts to reproduce near-bed hydrodynamic and sediment transport phenomena at a realistic scale. Experimental sediment transport studies in oscillating water tunnels have investigated the effect of wave skewness (e.g. Ribberink & Al-Salem 1994; Ahmed & Sato 2003; O'Donoghue & Wright 2004; Hassan & Ribberink 2005), wave asymmetry (e.g. King 1991; Watanabe & Sato 2004; van der A *et al.* 2010) and wave–current interaction (e.g. Dohmen-Janssen *et al.* 2002); the reader is referred to van der Werf *et al.* (2009) for a comprehensive summary of the available experimental data. An oscillating water tunnel consists of a U-shaped tube with a piston at one end that drives the fluid motion. Sediment is placed on the bottom of the horizontal portion of the tube, which has a typical length of about 5–15 m and a rectangular cross-section of dimensions 0.5–1 m. Due to its confined test section, oscillating water tunnels can produce fully turbulent oscillatory flows of velocities and periods comparable to those of real sea waves at a significantly smaller facility size than open wave flumes. In an oscillating water tunnel, the oscillatory motion produced by the piston propagates almost instantaneously along the entire tunnel. Consequently, unlike the wave motion in the sea or in a wave flume, flow in an oscillating water tunnel is uniform along the tunnel, and second-order wave propagation effects are absent. This has significant hydrodynamic implications, such as the absence of the conventional steady streaming arising from wave propagation (Longuet-Higgins 1953). However, note that streaming is still present in oscillating water tunnels as long as the flow does not consist of pure sinusoidal waves, as it is generated by the interaction between turbulence and mean velocity variations (Trowbridge & Madsen 1984*b*). Indeed, Ribberink & Al-Salem (1995) measured this streaming in experiments

involving skewed waves in the Delft oscillating water tunnel. Previous models of oscillating water tunnel streaming (Davies & Li 1997; Bosboom & Klopman 2000; Holmedal & Myrhaug 2006) focused on the near-bed region and did not quantify the observed streaming over the complete cross-section. Here, we show that the boundary-layer dynamics along all boundaries (bed, sidewalls and top) and the zero net flux requirement must be considered to predict the complete measured streaming profile, which results from a balance between the mean flow near the boundaries and an opposite mean flow in the central portion of the cross-section. The need to account for sidewall effects was already suggested by Holmedal & Myrhaug (2006).

These hydrodynamic differences between oscillating water tunnels and sea waves on sediment transport rates have generally been neglected in surf zone transport studies. Indeed, near-shore sediment transport models of propagating surf zone waves are commonly validated against oscillating water tunnel measurements. However, it has been shown that, at least in some cases, these hydrodynamic differences have an appreciable effect on sediment transport (Ribberink *et al.* 2008; Fuhrman *et al.* 2009; Holmedal & Myrhaug 2009; Yu, Hsu & Hanes 2010). Therefore, successful comparison between predictions of a sediment transport model and measurements in oscillating water tunnels does not guarantee the model's applicability to real wave conditions. Here we propose an analytical approach to prediction of bedload transport, which is specifically derived for oscillating water tunnels and consistently validated with oscillating water tunnel hydrodynamic and sediment transport measurements, as a sound first step in modelling near-shore sediment transport.

Prediction of bedload transport requires a correct characterization of the bed roughness. Most of the available laboratory sediment transport data correspond to sheet flow, a high-Shields-parameter transport regime in which a cloud of sediment is transported over an essentially flat bed. As shown in several sheet flow studies, the total hydraulic roughness that parametrizes the near-bed velocity is larger than the sediment diameter (e.g. Dohmen-Janssen, Hassan & Ribberink 2001; Hsu, Elgar & Guza 2006). While the hydraulic sheet flow roughness is parametrized by the total mobile-bed roughness, this is not necessarily the effective roughness with which to compute the bed shear stress responsible for transport. For example, accurate predictions of transport over rippled beds have been obtained by using $k_n = D_{50}$, instead of the total rippled bed hydraulic roughness (Madsen & Grant 1976). By analogy, it is conceivable that the effective bed shear stress that is responsible for sheet flow sediment transport is only a fraction of the total bed shear stress. The appropriate choice of sheet flow roughness to compute this effective bed shear stress remains an open question: some authors use the total hydraulic roughness (Ribberink 1998; Hsu *et al.* 2006), while others use an effective bed roughness of the order of the sediment diameter (Holmedal & Myrhaug 2006; Nielsen 2006). In a previous contribution (Gonzalez-Rodriguez & Madsen 2007), we proposed a simple conceptual model that yielded good bedload predictions for asymmetric and skewed waves when the bed roughness was parametrized by the sediment diameter. We later found that an extension of this model to describe transport under sinusoidal waves combined with a current (Gonzalez-Rodriguez & Madsen 2008) produced good predictions only when the roughness was parametrized by the total mobile-bed roughness, as proposed by Herrmann & Madsen (2007). Such inconsistency between the pure wave case and the wave-current case is attributed to insufficient accuracy of the hydrodynamic predictions of our previous conceptual model. The more rigorous analytical model presented in this paper overcomes this inconsistency and demonstrates that the

effective roughness should in all cases be parametrized by the total mobile-bed roughness.

In this paper, we present an analytical characterization of the boundary-layer flow in an oscillating water tunnel under asymmetric and skewed waves plus a weak collinear current. The model focuses on the case of rough, flat beds (sheet flow or fixed bed), while bedforms are not studied. In order to capture the physics of an oscillating water tunnel, the model assumes the waves to be non-propagating. The analytical boundary-layer model, which uses a time-varying eddy viscosity, is presented in § 2. To completely characterize the second-order hydrodynamics, geometrical effects for a typical tall and narrow section are considered in § 3. In § 4, we compare the hydrodynamic predictions of our model with experimental measurements. In § 5 the model's bed shear stress predictions are combined with a bedload formula to predict bedload sediment transport; the model's predictions are compared to experimental measurements of sheet flow transport in oscillating water tunnels for skewed waves, asymmetric waves and waves combined with a current.

2. Boundary-layer model

We present an analytical description of the boundary-layer hydrodynamics in an oscillating water tunnel, from which we obtain explicit closed-form expressions of the bed shear stresses. This analysis uses a space- and time-dependent eddy viscosity, following the previous work by Trowbridge & Madsen (1984*a*, *b*), which described the boundary-layer hydrodynamics under a propagating wave. Trowbridge and Madsen assumed a bilinear structure of the eddy viscosity and disregarded the finite thickness effect of the wave boundary layer. This simplification is not appropriate for the study of wave-induced mean flows in oscillating water tunnels, which are determined by the hydrodynamics of the whole tunnel section, as will be discussed below. Moreover, we are also interested in predicting cases where an externally imposed current is present. Thus, here we revisit the analysis of Trowbridge and Madsen with two improvements: (i) the possibility of an externally imposed current and (ii) a more sophisticated vertical structure that accounts for the finite thickness of the wave boundary layer and for the effects of the (imposed or wave-induced) current turbulence. In addition, while Trowbridge and Madsen considered the case of a propagating wave, here we restrict our analysis to a non-propagating wave, of relevance to oscillating water tunnel experiments. This allows us to obtain simple, explicit expressions for the bed shear stress, which are readily applicable to computation of bedload sediment transport.

We assume a spatial structure of the eddy viscosity that is consistent with previous eddy viscosity models. The magnitude of this eddy viscosity is determined through a closure hypothesis, which relates the time-average eddy viscosity and the time-average bed shear stress. The time dependence of the eddy viscosity is not assumed but inferred from the closure hypothesis; we show that accounting for this time dependence is necessary for a correct hydrodynamic description.

Since our analysis builds upon that of Trowbridge & Madsen (1984*a*, *b*), here we present only the main results and the key differences with Trowbridge and Madsen's work. For details of the derivation, the reader is referred to Trowbridge & Madsen (1984*a*, *b*) and Gonzalez-Rodriguez (2009).

2.1. *Governing equations*

We consider a two-dimensional, rough turbulent wave boundary layer. The ensemble-averaged boundary-layer velocities are denoted by (u, w), and the horizontal

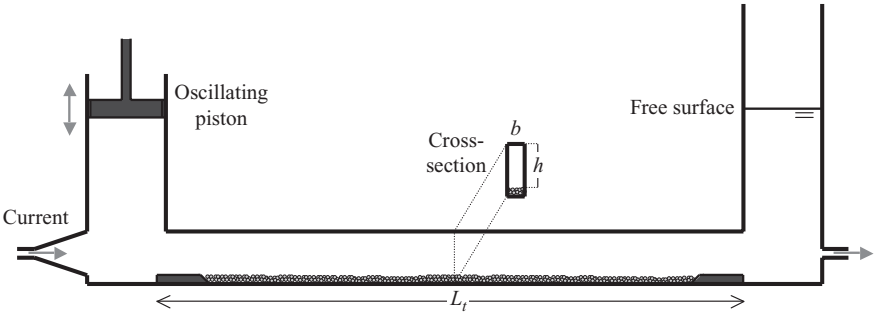

FIGURE 1. Sketch of an oscillating water tunnel. The oscillating motion in the test section is produced by the motion of a piston. In some facilities, a superimposed current can be prescribed by means of a pumping system. Sediment is placed on the bottom of the test section for transport studies.

free-stream velocity is denoted by u_b. By free-stream velocity we refer to the potential flow wave velocity at the outer edge of the boundary layer, which is imposed by the oscillatory motion of the piston. The vertical scale of the boundary layer is denoted by δ_w. For a propagating wave, the horizontal length scale is the inverse of the wavenumber, $1/k$; for an oscillating water tunnel, the horizontal length scale is the length of the experimental facility, L_t (see figure 1). The time scale is the wave period, $T = 2\pi/\omega$. In the general case of a propagating wave, flow inside the wave boundary layer is described by the continuity equation

$$\frac{\partial u}{\partial x} + \frac{\partial w}{\partial z} = 0, \tag{2.1}$$

and the boundary-layer momentum equation (Trowbridge 1983)

$$\frac{\partial u}{\partial t} + u\frac{\partial u}{\partial x} + w\frac{\partial u}{\partial z} = -\frac{1}{\rho}\frac{\partial p}{\partial x} + \frac{\partial}{\partial z}\frac{\tau_{zx}}{\rho} + O\left((k\delta_w)u_{bm}\omega\right). \tag{2.2}$$

Here, p denotes the free-stream pressure, u_{bm} is the maximum free-stream velocity, ρ is the fluid density and τ_{zx} is a component of the Reynolds shear stress tensor, given by

$$\tau_{zx} = \rho\nu_t\frac{\partial u}{\partial z}, \tag{2.3}$$

where $\nu_t(z, t)$ is the eddy viscosity, which is assumed isotropic but time-dependent.

In deriving (2.2), several assumptions have been made. First, the boundary-layer assumption requires that $k\delta_w \ll 1$. Second, the boundary-layer thickness must be large compared to the roughness elements, so that the details of flow around individual elements can be neglected. Thus, $\delta_w/D_n \gg 1$ is assumed, where D_n is the nominal sediment grain diameter or, more generally, the scale of the roughness protrusions. Third, flow is assumed to be rough and turbulent, so that the Reynolds stresses are much larger than the viscous stresses. Fourth, based on observations of steady turbulent flows, all components of the Reynolds stress tensor are assumed to be of the same order of magnitude.

In the case of an oscillating water tunnel studied here (see figure 1), the oscillatory motion propagates almost instantaneously along the tunnel, and the longitudinal scale is that of the experimental facility, L_t, which replaces $1/k$ in the previous equations. Oscillating water tunnels are very long, so that $\delta_w/L_t \ll 1$ and the boundary-layer assumption is satisfied. Further, $u_{bm}/(L_t\omega) \ll 1$, and the advective terms in (2.2) can

be neglected to yield

$$\frac{\partial u}{\partial t} = -\frac{1}{\rho}\frac{\partial p}{\partial x} + \frac{\partial}{\partial z}\frac{\tau_{zx}}{\rho} + O\left((\delta_w/L_t)u_{bm}\omega, u_{bm}^2/L_t\right). \tag{2.4}$$

The free-stream wave velocity will be represented by its two first Fourier harmonics,

$$u_b = u_{b1} + u_{b2} = \frac{U_\infty^{(1)}}{2}\,\mathrm{e}^{\mathrm{i}\omega t} + \frac{U_\infty^{(2)}}{2}\,\mathrm{e}^{\mathrm{i}2\omega t} + \text{c.c.}, \tag{2.5}$$

where c.c. denotes the complex conjugate. It is noted that (2.5) can describe a purely skewed wave (if the two harmonics are in phase), a purely asymmetric wave (if the two harmonics are in quadrature) or a combination of both, providing a reasonable approximation of surf zone waves. The shape of the near-bed velocity of a surf zone wave can be described using the asymmetry and skewed parameters $As = 1 - T_c/T$ and $Sk = 2u_c/U_b - 1$, where T_c is twice the elapsed time between the minimum and maximum near-bed velocities, u_c is the maximum onshore near-bed velocity and U_b is the crest-to-trough near-bed velocity height (Gonzalez-Rodriguez & Madsen 2007). Asymmetry and skewness of waves observed in the surf zone are in the range $0 \leqslant As \leqslant 2/3$ and $0 \leqslant Sk \leqslant 1/2$ (Elfrink, Hanes & Ruessink 2006). As discussed by Gonzalez-Rodriguez (2009), the two-harmonic approximation is only representative of real waves that are moderately asymmetric and skewed, with $0 \leqslant As \leqslant 1/3$ and $0 \leqslant Sk \leqslant 1/4$. The most common surf zone wave conditions, as well as most of the oscillating water tunnel experimental conditions, are within this allowable range or close to its upper bound.

The second velocity harmonic is assumed small compared to the first, so that

$$\lambda \equiv \frac{\left|U_\infty^{(2)}\right|}{\left|U_\infty^{(1)}\right|} \ll 1. \tag{2.6}$$

We account for the possibility of an imposed current, which is assumed weak compared to the wave, so that

$$\hat{\lambda} \equiv \left(\frac{u_{*c}}{u_{*w}}\right)^2 \ll 1, \tag{2.7}$$

where u_{*w} and u_{*c} are the wave and current shear velocities, respectively, which are related to the wave and current shear stresses by

$$u_{*w} = \frac{\overline{|\tau_{bw}|^{1/2}}}{\sqrt{\rho}}, \tag{2.8}$$

$$u_{*c} = \frac{|\tau_{bc}|^{1/2}}{\sqrt{\rho}}, \tag{2.9}$$

where hereafter the overline denotes a time average. We also define a combined wave-current shear velocity as

$$u_{*wc} = \frac{\overline{|\tau_b|^{1/2}}}{\sqrt{\rho}} = \frac{\overline{|\tau_{bw} + \tau_{bc}|^{1/2}}}{\sqrt{\rho}}. \tag{2.10}$$

In order to keep both the second-harmonic effect and the current effect in the analysis, they are assumed to be of the same order of magnitude, that is,

$$\lambda \sim \hat{\lambda}. \tag{2.11}$$

The variables are decomposed into a mean, even harmonics and odd harmonics

$$u = \overline{u} + \tilde{u}_o + \tilde{u}_e, \tag{2.12}$$

$$p = \overline{p} + \tilde{p}_o + \tilde{p}_e, \tag{2.13}$$

$$\nu_t = \overline{\nu} + \tilde{\nu}_o + \tilde{\nu}_e. \tag{2.14}$$

Then, (2.4) can be written as

$$\frac{\partial (\tilde{u}_o + \tilde{u}_e)}{\partial t} = -\frac{1}{\rho}\frac{\partial}{\partial x}(\overline{p} + \tilde{p}_o + \tilde{p}_e) + \frac{\partial}{\partial z}\left[(\overline{\nu} + \tilde{\nu}_o + \tilde{\nu}_e)\frac{\partial}{\partial z}(\overline{u} + \tilde{u}_o + \tilde{u}_e)\right]. \tag{2.15}$$

As will be discussed below, while the horizontal mean pressure gradient is small, it must be kept in (2.15), even in the absence of a current, in order to satisfy the total flow rate constraint imposed in the tunnel (the flow rate must be zero if no current is imposed). To indicate that this pressure gradient is a constant, we denote it by

$$\overline{G} \equiv \frac{\partial \overline{p}}{\partial x}. \tag{2.16}$$

Time averaging (2.15) yields

$$0 = -\frac{\overline{G}}{\rho} + \frac{\partial}{\partial z}\left[\overline{\nu}\frac{\partial \overline{u}}{\partial z} + \overline{\tilde{\nu}_o \frac{\partial \tilde{u}_o}{\partial z}} + \overline{\tilde{\nu}_e \frac{\partial \tilde{u}_e}{\partial z}}\right]. \tag{2.17}$$

Subtracting (2.17) from (2.15) and separating odd and even harmonics yield, to second order,

$$\frac{\partial \tilde{u}_o}{\partial t} = -\frac{1}{\rho}\frac{\partial \tilde{p}_o}{\partial x} + \frac{\partial}{\partial z}\left[(\overline{\nu} + \tilde{\nu}_e)\frac{\partial \tilde{u}_o}{\partial z}\right] \tag{2.18}$$

and

$$\frac{\partial \tilde{u}_e}{\partial t} = -\frac{1}{\rho}\frac{\partial \tilde{p}_e}{\partial x} + \frac{\partial}{\partial z}\left[\tilde{\nu}_o \frac{\partial \tilde{u}_o}{\partial z} - \overline{\tilde{\nu}_o \frac{\partial \tilde{u}_o}{\partial z}}\right] + \frac{\partial}{\partial z}\left[\tilde{\nu}_e \frac{\partial \tilde{u}_e}{\partial z} - \overline{\tilde{\nu}_e \frac{\partial \tilde{u}_e}{\partial z}}\right] + \frac{\partial}{\partial z}\left[\overline{\nu}\frac{\partial \tilde{u}_e}{\partial z}\right] + \frac{\partial}{\partial z}\left[\tilde{\nu}_e \frac{\partial \overline{u}}{\partial z}\right]. \tag{2.19}$$

2.2. *The eddy viscosity structure*

Following Trowbridge & Madsen (1984*b*), the eddy viscosity is assumed to depend both on the distance from the boundary (z) and on time, according to

$$\nu_t(z, t) = \overline{\nu}(z)\left(\frac{1}{2} + \frac{a^{(1)}}{2}\mathrm{e}^{\mathrm{i}\omega t} + \frac{a^{(2)}}{2}\mathrm{e}^{\mathrm{i}2\omega t} + \text{c.c.} + O(\epsilon^2)\right), \tag{2.20}$$

where $\epsilon \sim |u^{(3)}/u^{(1)}| \ll 1$. In order to account for current turbulence, a vertical structure different from Trowbridge & Madsen's is assumed. Based on law-of-the-wall arguments applied to both the wave boundary layer (of thickness δ_w) and the current boundary layer (of thickness δ_c), the vertical structure of the eddy viscosity, $\overline{\nu}(z)$, is assumed to be

$$\overline{\nu}(z) = \begin{cases} \kappa u_{*wc} z, & 0 \leqslant z \leqslant \delta_I, \\ \kappa u_{*wc}\delta_I, & \delta_I < z \leqslant \delta_J, \\ \kappa u_{*c} z, & \delta_J < z \leqslant \delta_K, \\ \kappa u_{*c}\delta_L, & \delta_K < z, \end{cases} \tag{2.21}$$

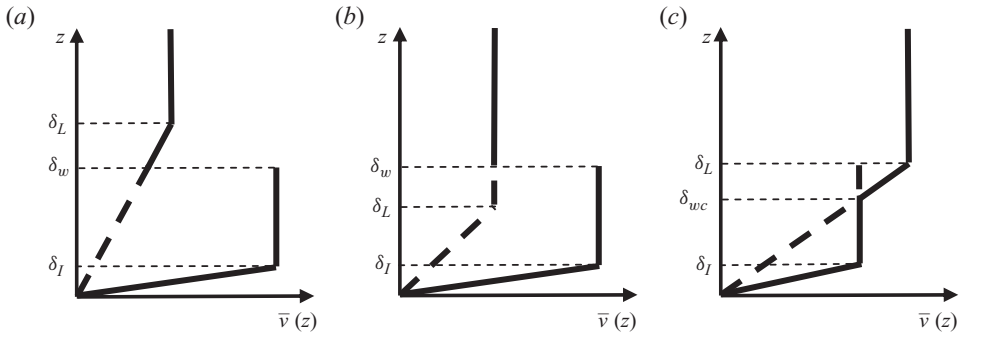

FIGURE 2. Illustration of different possible cases of the eddy viscosity vertical structure, as defined by (2.21), with u_{*c}/u_{*wc} increasing from left to right.

where $\delta_I \equiv \delta_w/6$, $\delta_L \equiv \delta_c/6$, $\delta_{wc} \equiv u_{*wc}\delta_I/u_{*c}$,

$$\delta_J \equiv \begin{cases} \min(\delta_w, \delta_{wc}), & \text{if } u_{*wc}\delta_I < u_{*c}\delta_L, \\ \delta_w, & \text{if } u_{*wc}\delta_I \geqslant u_{*c}\delta_L, \end{cases} \tag{2.22}$$

$\delta_K \equiv \max(\delta_J, \delta_L)$ and $\kappa \approx 0.4$ is von Kármán's constant. The wave boundary-layer thickness is given by $\delta_w \equiv Al$, where l, the boundary-layer length scale, is defined by

$$l \equiv \frac{\kappa u_{*wc}}{\omega}. \tag{2.23}$$

The computation of A, a function of the relative roughness, is discussed in § 2.6. The assumption given by (2.21) is based on a conceptualization of the wave and current boundary layers as divided into two regions. In the lower region, which corresponds to the bottom 1/6 of the layer, the size of the turbulent eddies increases with the distance from the wall. In the upper region, the size of the turbulent eddies becomes constant. Such an assumption accurately reproduces velocity measurements in steady turbulent flows (Clauser 1956).

The vertical structures of the eddy viscosity defined by (2.21) are illustrated in figure 2 with u_{*c}/u_{*wc} increasing from left to right.

2.3. *The generic ordinary differential equation*

To solve the boundary-layer equations, (2.17)–(2.19), we will decompose the even and odd parts of the velocity into a series of even and odd Fourier harmonics, respectively, and solve harmonic by harmonic (up to the third harmonic). For each harmonic ($n = 1, 2, 3$) we will obtain an ordinary differential equation that we need to solve. These differential equations are all similar and can be written in a generic form. Due to a different eddy viscosity assumption, this generic differential equation is different from that discussed by Trowbridge & Madsen (1984*a*, *b*). In this section, we present the solution of this generic ordinary differential equation, which will later be repeatedly used to describe the boundary-layer hydrodynamics. Given the assumed vertical structure of the eddy viscosity, the differential equation that arises when

studying the nth harmonic is of the form

$$\left.\begin{aligned}
&\frac{\mathrm{d}}{\mathrm{d}\zeta}\left(\zeta\frac{\mathrm{d}F^{(n)}}{\mathrm{d}\zeta}\right)-\mathrm{i}nF^{(n)}=0, && 0\leqslant\zeta\leqslant\frac{\delta_I}{l},\\
&\frac{\delta_I}{l}\frac{\mathrm{d}^2F^{(n)}}{\mathrm{d}\zeta^2}-\mathrm{i}nF^{(n)}=0, && \frac{\delta_I}{l}<\zeta\leqslant\frac{\delta_J}{l},\\
&\frac{u_{*c}}{u_{*wc}}\frac{\mathrm{d}}{\mathrm{d}\zeta}\left(\zeta\frac{\mathrm{d}F^{(n)}}{\mathrm{d}\zeta}\right)-\mathrm{i}nF^{(n)}=0, && \frac{\delta_J}{l}<\zeta\leqslant\frac{\delta_K}{l},\\
&\frac{u_{*c}}{u_{*wc}}\frac{\delta_L}{l}\frac{\mathrm{d}^2F^{(n)}}{\mathrm{d}\zeta^2}-\mathrm{i}nF^{(n)}=0, && \frac{\delta_K}{l}<\zeta,
\end{aligned}\right\} \tag{2.24}$$

where $\zeta\equiv z/l$ is the non-dimensional vertical coordinate and $n\in\mathbb{N}$. $F^{(n)}(\zeta)$ is the complex solution of (2.24) for a given value of n. At the outer edge of the boundary layer, the velocity must converge to the prescribed potential flow velocity, which, as shown below, requires that $F^{(n)}\to 0$ as $\zeta\to\infty$. The solution is

$$F^{(n)}=\begin{cases}
[\ker(2\sqrt{n\zeta})+\mathrm{i}\,\mathrm{kei}(2\sqrt{n\zeta})] & \\
\quad +A^{(n)}[\mathrm{ber}(2\sqrt{n\zeta})+\mathrm{i}\,\mathrm{bei}(2\sqrt{n\zeta})], & 0\leqslant\zeta\leqslant\dfrac{\delta_I}{l},\\
B^{(n)}\exp\left\{-\mathrm{e}^{\mathrm{i}\pi/4}\sqrt{\dfrac{nl}{\delta_I}}\left(\zeta-\dfrac{\delta_I}{l}\right)\right\} & \\
\quad +C^{(n)}\exp\left\{\mathrm{e}^{\mathrm{i}\pi/4}\sqrt{\dfrac{nl}{\delta_I}}\left(\zeta-\dfrac{\delta_I}{l}\right)\right\}, & \dfrac{\delta_I}{l}<\zeta\leqslant\dfrac{\delta_J}{l},\\
D^{(n)}[\ker(2\sqrt{\tilde{n}\zeta})+\mathrm{i}\,\mathrm{kei}(2\sqrt{\tilde{n}\zeta})] & \\
\quad +E^{(n)}[\mathrm{ber}(2\sqrt{\tilde{n}\zeta})+\mathrm{i}\,\mathrm{bei}(2\sqrt{\tilde{n}\zeta})], & \dfrac{\delta_J}{l}<\zeta\leqslant\dfrac{\delta_K}{l},\\
H^{(n)}\exp\left\{-\mathrm{e}^{\mathrm{i}\pi/4}\sqrt{\dfrac{\tilde{n}l}{\delta_L}}\left(\zeta-\dfrac{\delta_K}{l}\right)\right\}, & \dfrac{\delta_K}{l}<\zeta,
\end{cases} \tag{2.25}$$

with $\tilde{n}\equiv nu_{*wc}/u_{*c}$; ker, kei, ber and bei denote Kelvin functions of order zero (Abramowitz & Stegun 1965). In order to guarantee the continuity of velocities and shear stresses, we must impose that F and $\nu\,\mathrm{d}F/\mathrm{d}\zeta$ are continuous. This yields six conditions, from which the six unknown constants, $A^{(n)}$, $B^{(n)}$, $C^{(n)}$, $D^{(n)}$, $E^{(n)}$ and $H^{(n)}$, are determined (see Gonzalez-Rodriguez 2009 for details)

$$A^{(n)}=\alpha_{AH}H^{(n)}, \tag{2.26}$$
$$B^{(n)}=\alpha_{BH}H^{(n)}, \tag{2.27}$$
$$C^{(n)}=\alpha_{CH}H^{(n)}, \tag{2.28}$$
$$D^{(n)}=\alpha_{DH}H^{(n)}, \tag{2.29}$$
$$E^{(n)}=\alpha_{EH}H^{(n)}, \tag{2.30}$$
$$H^{(n)}=\frac{\ker C_I+\mathrm{i}\,\mathrm{kei}\,C_I}{\alpha_{BH}+\alpha_{CH}-\alpha_{AH}\,[\mathrm{ber}\,C_I+\mathrm{i}\,\mathrm{bei}\,C_I]}, \tag{2.31}$$

where

$$\begin{aligned}
\alpha_{AH}=&\{(\alpha_{BH}+\alpha_{CH})\,[-\mathrm{i}\ker_1 C_I+\mathrm{kei}_1 C_I]-(-\alpha_{BH}+\alpha_{CH})\,[\ker C_I+\mathrm{i}\,\mathrm{kei}\,C_I]\}\\
&\{[\mathrm{ber}\,C_I+\mathrm{i}\,\mathrm{bei}\,C_I]\,[-\mathrm{i}\ker_1 C_I+\mathrm{kei}_1 C_I]\\
&-[-\mathrm{i}\,\mathrm{ber}_1 C_I+\mathrm{bei}_1 C_I]\,[\ker C_I+\mathrm{i}\,\mathrm{kei}\,C_I]\}^{-1},
\end{aligned} \tag{2.32}$$

$$\alpha_{BH} = \frac{1}{2\exp\{-K_I(\delta_J-\delta_I)/l\}} \left\{\alpha_{DH}\left[(\ker\tilde{C}_J + \mathrm{i}\,\mathrm{kei}\,\tilde{C}_J) - \sqrt{\frac{u_{*c}\delta_J}{u_{*wc}\delta_I}}(-\mathrm{i}\,\mathrm{ker}_1\,\tilde{C}_J + \mathrm{kei}_1\tilde{C}_J)\right] + \alpha_{EH}\left[(\mathrm{ber}\,\tilde{C}_J + \mathrm{i}\,\mathrm{bei}\,\tilde{C}_J) - \sqrt{\frac{u_{*c}\delta_J}{u_{*wc}\delta_I}}(-\mathrm{i}\,\mathrm{ber}_1\tilde{C}_J + \mathrm{bei}_1\tilde{C}_J)\right]\right\}, \tag{2.33}$$

$$\alpha_{CH} = \frac{1}{2\exp\{K_I(\delta_J-\delta_I)/l\}} \left\{\alpha_{DH}\left[(\ker\tilde{C}_J + \mathrm{i}\,\mathrm{kei}\,\tilde{C}_J) + \sqrt{\frac{u_{*c}\delta_J}{u_{*wc}\delta_I}}(-\mathrm{i}\,\mathrm{ker}_1\,\tilde{C}_J + \mathrm{kei}_1\tilde{C}_J)\right] + \alpha_{EH}\left[(\mathrm{ber}\,\tilde{C}_J + \mathrm{i}\,\mathrm{bei}\,\tilde{C}_J) + \sqrt{\frac{u_{*c}\delta_J}{u_{*wc}\delta_I}}(-\mathrm{i}\,\mathrm{ber}_1\tilde{C}_J + \mathrm{bei}_1\tilde{C}_J)\right]\right\}, \tag{2.34}$$

$$\alpha_{DH} = \left\{[-\mathrm{i}\,\mathrm{ber}_1\tilde{C}_k + \mathrm{bei}_1\tilde{C}_k] + \sqrt{\delta_L/\delta_K}[\mathrm{ber}\tilde{C}_k + \mathrm{i}\,\mathrm{bei}\,\tilde{C}_k]\right\} \{[-\mathrm{i}\,\mathrm{ber}_1\tilde{C}_k + \mathrm{bei}_1\tilde{C}_k][\ker\tilde{C}_k + \mathrm{i}\,\mathrm{kei}\,\tilde{C}_k] + [\mathrm{ber}\tilde{C}_k + \mathrm{i}\,\mathrm{bei}\tilde{C}_k][\mathrm{i}\,\mathrm{ker}_1\,\tilde{C}_k - \mathrm{kei}_1\tilde{C}_k]\}^{-1}, \tag{2.35}$$

$$\alpha_{EH} = \left\{[-\mathrm{i}\,\mathrm{ker}_1\,\tilde{C}_k + \mathrm{kei}_1\tilde{C}_k] + \sqrt{\delta_L/\delta_K}[\ker\tilde{C}_k + \mathrm{i}\,\mathrm{kei}\,\tilde{C}_k]\right\} \{[\mathrm{i}\,\mathrm{ber}_1\tilde{C}_k - \mathrm{bei}_1\tilde{C}_k][\ker\tilde{C}_k + \mathrm{i}\,\mathrm{kei}\,\tilde{C}_k] + [\mathrm{ber}\,\tilde{C}_k + \mathrm{i}\,\mathrm{bei}\,\tilde{C}_k][-\mathrm{i}\,\mathrm{ker}_1\,\tilde{C}_k + \mathrm{kei}_1\tilde{C}_k]\}^{-1}, \tag{2.36}$$

where ker_1, kei_1, ber_1 and bei_1 are the Kelvin functions of order 1 (Abramowitz & Stegun 1965) and

$$C_I \equiv 2\sqrt{\frac{n\delta_I}{l}}, \tag{2.37}$$

$$\tilde{C}_J \equiv 2\sqrt{\frac{\tilde{n}\delta_J}{l}}, \tag{2.38}$$

$$\tilde{C}_K \equiv 2\sqrt{\frac{\tilde{n}\delta_K}{l}}, \tag{2.39}$$

$$K_I \equiv \mathrm{e}^{\mathrm{i}\pi/4}\sqrt{\frac{nl}{\delta_I}}. \tag{2.40}$$

2.4. *First-order analysis*

We first consider the leading-order terms, $O(\lambda^0) \sim O(\hat{\lambda}^0) \sim O(1)$. Only the odd equation, (2.18), includes leading-order terms. Therefore, the governing leading-order equation is

$$\frac{\partial\tilde{u}_o}{\partial t} = \frac{\partial u_{b1}}{\partial t} + \frac{\partial}{\partial z}\left[(\overline{\nu} + \tilde{\nu}_e)\frac{\partial\tilde{u}_o}{\partial z}\right]. \tag{2.41}$$

The ratio between the third and first harmonics of the velocity is anticipated to be

$$\left|\frac{u^{(3)}}{u^{(1)}}\right| \sim \frac{\nu^{(2)}}{\overline{\nu}} \sim a^{(2)} \sim \epsilon \sim 0.4 \gg \lambda \sim \hat{\lambda}. \tag{2.42}$$

This scaling will be confirmed once we obtain an expression for $a^{(2)}$, (2.58). We neglect terms of $O(\epsilon^2)$. The first-order variables read

$$\overline{\nu} = \overline{\nu}(z), \tag{2.43}$$

$$\tilde{\nu}_e = \overline{\nu}(z)\left(\frac{a^{(2)}}{2}\,\mathrm{e}^{\mathrm{i}2\omega t} + \text{c.c.} + O(\epsilon^2)\right), \tag{2.44}$$

$$\tilde{u}_o = \left(\frac{u^{(1)}}{2}\,\mathrm{e}^{\mathrm{i}\omega t} + \frac{u^{(3)}}{2}\,\mathrm{e}^{\mathrm{i}3\omega t} + \text{c.c.}\right) + O\left(\epsilon^2 u^{(1)}\right). \tag{2.45}$$

2.4.1. *First-order, first-harmonic solution*

The governing equation for the first harmonic is

$$\mathrm{i}\omega u^{(1)} = \mathrm{i}\omega U_\infty^{(1)} + \frac{\mathrm{d}}{\mathrm{d}z}\left(\overline{\nu}\left(\frac{\mathrm{d}u^{(1)}}{\mathrm{d}z} + \frac{a^{(2)}}{2}\frac{\mathrm{d}u^{(1)*}}{\mathrm{d}z}\right)\right), \tag{2.46}$$

identical to that obtained by Trowbridge & Madsen (1984*a*, *b*). The symbol * indicates complex conjugation. By solving this equation we obtain the first-order velocity

$$u^{(1)} = U_\infty^{(1)}\left(1 - \frac{F^{(1)}(\zeta)}{F^{(1)}(\zeta_0)}\right) + \frac{a^{(2)}}{4}U_\infty^{(1)*}\left(\frac{F^{(1)*}(\zeta)}{F^{(1)*}(\zeta_0)} - \frac{F^{(1)}(\zeta)}{F^{(1)}(\zeta_0)}\right), \tag{2.47}$$

where the second term is of order ϵ with respect to the first and terms of order ϵ^2 are neglected. While this expression is analogous to Trowbridge & Madsen's, it is noted that our function F is different from theirs, due to our different eddy viscosity assumption.

The first-harmonic shear stress is given by

$$\frac{\tau^{(1)}}{\rho} = \overline{\nu}\left(\frac{\mathrm{d}u^{(1)}}{\mathrm{d}z} + \frac{a^{(2)}}{2}\frac{\mathrm{d}u^{(1)*}}{\mathrm{d}z}\right). \tag{2.48}$$

To compute the first-harmonic bed shear stress, we use the approximation (Trowbridge & Madsen 1984*a*)

$$\lim_{\zeta\to\zeta_0}\zeta\frac{\mathrm{d}F^{(n)}}{\mathrm{d}\zeta} \approx \lim_{\zeta\to 0}\zeta\frac{\mathrm{d}F^{(n)}}{\mathrm{d}\zeta} = -\frac{1}{2}, \tag{2.49}$$

to obtain

$$\frac{\tau_b^{(1)}}{\rho} = \frac{\kappa}{2}\frac{u_{*wc}U_\infty^{(1)}}{F^{(1)}(\zeta_0)} + \frac{\kappa u_{*wc}}{8}a^{(2)}U_\infty^{(1)*}\frac{F^{(1)}(\zeta_0) + F^{(1)*}(\zeta_0)}{|F^{(1)}(\zeta_0)|^2}, \tag{2.50}$$

where the second term is of order ϵ with respect to the first. The error introduced by (2.49) depends on the relative roughness. For a small roughness of $\zeta_0 = 0.001$ (a typical value for a fine-grain, fixed-bed case), the error introduced by (2.49) is less than 0.5 % in magnitude and 1° in phase. For a large roughness of $\zeta_0 = 0.05$ (a typical value for a coarse-grain, mobile-bed case), the error introduced by (2.49) is 9 % in magnitude and 9° in phase for the first harmonic ($n = 1$) and 17 % and 18° for the third harmonic ($n = 3$). Therefore, (2.50) is a good approximation to the bed shear stress when the roughness is not too large. For a more accurate computation when large roughnesses are involved, $\mathrm{d}F^{(n)}/\mathrm{d}\zeta$ must be evaluated at ζ_0, which is easily done numerically.

2.4.2. *First-order, third-harmonic solution*

The governing equation for the third harmonic is

$$3\mathrm{i}\omega u^{(3)} = \frac{\mathrm{d}}{\mathrm{d}z}\left[\overline{\nu}\left(\frac{\mathrm{d}u^{(3)}}{\mathrm{d}z} + \frac{a^{(2)}}{2}\frac{\mathrm{d}u^{(1)}}{\mathrm{d}z}\right)\right]. \tag{2.51}$$

The solution is

$$u^{(3)} = \frac{a^{(2)}}{4}U_\infty^{(1)}\left(-\frac{F^{(1)}(\zeta)}{F^{(1)}(\zeta_0)} + \frac{F^{(3)}(\zeta)}{F^{(3)}(\zeta_0)}\right), \tag{2.52}$$

which again differs from Trowbridge & Madsen's (1984*a*, *b*) in our different definition of F.

The leading-order, third-harmonic shear stress is given by

$$\frac{\tau^{(3)}}{\rho} = \overline{\nu}\left(\frac{\mathrm{d}u^{(3)}}{\mathrm{d}z} + \frac{a^{(2)}}{2}\frac{\mathrm{d}u^{(1)}}{\mathrm{d}z}\right). \tag{2.53}$$

By using the approximation given by (2.49), we obtain

$$\frac{\tau_b^{(3)}}{\rho} = \frac{\kappa u_{*wc} a^{(2)} U_\infty^{(1)}}{8}\frac{[3F^{(3)}(\zeta_0) - F^{(1)}(\zeta_0)]}{F^{(1)}(\zeta_0)F^{(3)}(\zeta_0)}. \tag{2.54}$$

As discussed above, (2.54) should not be used for large roughnesses.

2.4.3. *Determination of u_{*wc} and $a^{(2)}$*

To close the first-order solution, we need to determine u_{*wc} to second order (ϵ^1) and $a^{(2)}$ to leading order (ϵ^0). For this, we follow Trowbridge & Madsen (1984*a*) and impose

$$u_{*wc} = \overline{\left|\frac{\tau_b}{\rho}\right|^{1/2}}, \tag{2.55}$$

$$u_{*wc}a^{(2)} = 2\overline{\mathrm{e}^{-\mathrm{i}2\omega t}\left|\frac{\tau_b}{\rho}\right|^{1/2}}, \tag{2.56}$$

to obtain

$$u_{*wc} = \frac{\kappa}{2\pi}\frac{\Gamma^2(3/4)}{\Gamma^2(5/4)}\frac{\left|U_\infty^{(1)}\right|}{|F^{(1)}(\zeta_0)|} \mathrm{Re}\left\{1 + \frac{a^{(2)}U_\infty^{(1)*}}{U_\infty^{(1)}}\left[\frac{1}{4} - \frac{1}{5}\frac{F^{(1)}(\zeta_0)}{F^{(1)*}(\zeta_0)} + \frac{3}{20}\frac{F^{(1)}(\zeta_0)F^{(1)}(\zeta_0)}{F^{(1)*}(\zeta_0)F^{(3)}(\zeta_0)}\right] + O(\epsilon^2)\right\} \tag{2.57}$$

and

$$a^{(2)} = \frac{2}{5}\frac{U_\infty^{(1)}}{U_\infty^{(1)*}}\frac{F^{(1)*}(\zeta_0)}{F^{(1)}(\zeta_0)}[1 + O(\epsilon)], \tag{2.58}$$

which confirms that $\epsilon \sim a^{(2)} \sim 2/5$.

2.4.4. *Determination of ζ_0*

The value of $\zeta_0 \equiv z_0/l$, the non-dimensional vertical location of the zero velocity, depends through l on the wave-current shear velocity, u_{*wc}, which in turn depends on ζ_0. For a rough turbulent flow, ζ_0 is defined by

$$z_0 = \frac{k_n}{30}, \tag{2.59}$$

$$\zeta_0 = \frac{z_0}{l} = \frac{k_n \omega}{30\kappa u_{*wc}}. \tag{2.60}$$

For a smooth turbulent flow, ζ_0 is defined by

$$z_0 = \frac{\nu_{molec}}{9u_{*wc}}, \tag{2.61}$$

$$\zeta_0 = \frac{z_0}{l} = \frac{\nu_{molec}\omega}{9\kappa u_{*wc}}, \tag{2.62}$$

where ν_{molec} is the molecular kinematic viscosity. By using the solution for u_{*wc} given by (2.57), we obtain the following implicit equation for ζ_0, which can be solved by iteration:

$$\left|F^{(1)}(\zeta_0)\right| - \zeta_0\alpha\left(\frac{\Gamma(3/4)}{\Gamma(5/4)}\right)^2 \left|U_\infty^{(1)}\right| \mathrm{Re}\left\{1 + \frac{2}{5}\frac{F^{(1)}(\zeta_0)}{F^{(1)*}(\zeta_0)}\left[\frac{1}{4} - \frac{1}{5}\frac{F^{(1)}(\zeta_0)}{F^{(1)*}(\zeta_0)} + \frac{3}{20}\frac{F^{(1)}(\zeta_0)F^{(1)}(\zeta_0)}{F^{(1)*}(\zeta_0)F^{(3)}(\zeta_0)}\right]\right\} = 0, \tag{2.63}$$

where $\alpha = 15\kappa^2/(\pi\omega k_n)$ or $\alpha = 9\kappa^3/(4\pi^2\omega\nu_{molec})$ for rough or smooth turbulent flow, respectively. Once ζ_0 is known, (2.60) or (2.62) is used to compute u_{*wc}. We note that viscous stresses were neglected at every depth in the governing equations, thus assuming a rough turbulent flow. In the case of a smooth turbulent flow, the effect of the thin viscous sublayer is thus neglected.

2.5. *Second-order analysis*

Next, we consider the second-order terms, of order λ or $\hat{\lambda}$. We neglect all terms of higher order, such as terms of order $\lambda\epsilon$ or $\hat{\lambda}\epsilon$. These higher-order terms are of the same order as the fourth harmonic of the velocity and the third harmonic of the eddy viscosity, which have also been neglected. The odd-harmonic equation, (2.18), has no term of $O(\lambda) \sim O(\hat{\lambda})$, while the time-average and the even-harmonic equations, (2.17) and (2.19), do. These two latter equations yield the zeroth- and second-harmonic solutions, respectively.

At this order, our analysis diverges from Trowbridge & Madsen's (1984*a*, *b*), since in their analysis the current effects are neglected and the terms of order $\hat{\lambda}$ are absent. In addition, since our analysis does not consider propagating waves, simple explicit expressions of the second-harmonic solution can be obtained here.

2.5.1. *Second-order, zeroth-harmonic solution*

The governing equation is

$$0 = -\frac{1}{\rho}\frac{\partial \overline{p}}{\partial x} + \frac{\partial}{\partial z}\left[\overline{\nu}\frac{\partial \overline{u}}{\partial z} + \overline{\tilde{\nu}_o \frac{\partial \tilde{u}_o}{\partial z}}\right]. \tag{2.64}$$

The longitudinal pressure gradient due to the imposed or wave-induced current varies over the length scale of the oscillating water tunnel, and therefore it can be treated as a constant, $\overline{G} \equiv \partial\overline{p}/\partial x$. Thus,

$$\frac{\mathrm{d}}{\mathrm{d}z}\left[\frac{\overline{\tau}}{\rho}\right] = \frac{\mathrm{d}}{\mathrm{d}z}\left[\overline{\nu}\left(\frac{\mathrm{d}\overline{u}}{\mathrm{d}z} + \frac{a^{(1)}}{4}\frac{\mathrm{d}u^{(1)*}}{\mathrm{d}z} + \frac{a^{(1)*}}{4}\frac{\mathrm{d}u^{(1)}}{\mathrm{d}z}\right)\right] = \frac{\overline{G}}{\rho}. \tag{2.65}$$

Therefore, the mean shear stress is

$$\overline{\tau} = \overline{G}(z - z_0) + \overline{\tau}_b, \tag{2.66}$$

where $\overline{\tau}_b$ is the unknown mean bed shear stress. Since Trowbridge & Madsen (1984*a*, *b*) neglected current effects, in their analysis $\overline{G}=0$. Integration of (2.65) with the boundary condition $\overline{u}(z_0)=0$ yields

$$\overline{u} = -\mathrm{Re}\left\{\frac{a^{(1)*}}{2}U_\infty^{(1)}\left(1-\frac{F^{(1)}(\zeta)}{F^{(1)}(\zeta_0)}\right)\right\} + I(z), \tag{2.67}$$

where $I(z)$ is defined by

$$I(z) \equiv \frac{1}{\rho}\int_{z_0}^{z}\frac{1}{\overline{\nu}(z')}[\overline{G}(z'-z_0)+\overline{\tau}_b]\,\mathrm{d}z'. \tag{2.68}$$

With the mean eddy viscosity given by (2.21), evaluation of the integral (2.68) results in

$$I(z) = \begin{cases} \dfrac{1}{\rho\kappa u_{*wc}}\left[\overline{G}(z-z_0)+(\overline{\tau}_b-z_0\overline{G})\ln\dfrac{z}{z_0}\right], & z \leqslant \delta_I \\ I(\delta_I)+\dfrac{1}{\rho\kappa u_{*wc}\delta_I}\left[\overline{G}\dfrac{z^2-\delta_I^2}{2}+(\overline{\tau}_b-z_0\overline{G})(z-\delta_I)\right], & \delta_I < z \leqslant \delta_J \\ I(\delta_J)+\dfrac{1}{\rho\kappa u_{*c}}\left[\overline{G}(z-\delta_J)+(\overline{\tau}_b-z_0\overline{G})\ln\dfrac{z}{\delta_J}\right], & \delta_J < z \leqslant \delta_K \\ I(\delta_K)+\dfrac{1}{\rho\kappa u_{*c}\delta_L}\left[\overline{G}\dfrac{z^2-\delta_K^2}{2}+(\overline{\tau}_b-z_0\overline{G})(z-\delta_K)\right], & \delta_K < z. \end{cases} \tag{2.69}$$

2.5.2. *Second-order, second-harmonic solution*

The governing equation for the second harmonic reads

$$\frac{\partial\tilde{u}_e}{\partial t} = \frac{\partial u_{b2}}{\partial t}+\frac{\partial}{\partial z}\left[\tilde{\nu}_o\frac{\partial\tilde{u}_o}{\partial z}-\overline{\tilde{\nu}_o\frac{\partial\tilde{u}_o}{\partial z}}\right]+\frac{\partial}{\partial z}\left[\overline{\nu}\frac{\partial\tilde{u}_e}{\partial z}\right], \tag{2.70}$$

which, in terms of Fourier harmonics, becomes

$$\frac{\mathrm{d}}{\mathrm{d}z}\left(\overline{\nu}\frac{\mathrm{d}u^{(2)}}{\mathrm{d}z}\right)-2\mathrm{i}\omega u^{(2)} = -2\mathrm{i}\omega U_\infty^{(2)}-\frac{\mathrm{d}}{\mathrm{d}z}\left(\overline{\nu}\frac{a^{(1)}}{2}\frac{\mathrm{d}u^{(1)}}{\mathrm{d}z}\right), \tag{2.71}$$

where, for brevity, the complex conjugate terms (c.c.) have been omitted on both sides. Next, we introduce the first-order solution, (2.47), into (2.71), retaining the first-order terms only. This resulting equation is of the type discussed in § 2.3. By applying the bottom boundary condition, $u^{(2)}(\zeta_0)=0$, we obtain

$$u^{(2)} = U_\infty^{(2)}\left(1-\frac{F^{(2)}(\zeta)}{F^{(2)}(\zeta_0)}\right)+\frac{a^{(1)}}{2}U_\infty^{(1)}\left(\frac{F^{(2)}(\zeta)}{F^{(2)}(\zeta_0)}-\frac{F^{(1)}(\zeta)}{F^{(1)}(\zeta_0)}\right). \tag{2.72}$$

The leading-order, second-harmonic shear stress is given by

$$\frac{\tau^{(2)}}{\rho} = \overline{\nu}\left(\frac{a^{(1)}}{2}\frac{\mathrm{d}u^{(1)}}{\mathrm{d}z}+\frac{\mathrm{d}u^{(2)}}{\mathrm{d}z}\right). \tag{2.73}$$

By using the approximation given by (2.49), we obtain

$$\frac{\tau_b^{(2)}}{\rho} = \frac{\kappa u_{*wc}}{4}\left[a^{(1)}U_\infty^{(1)}\frac{[2F^{(2)}(\zeta_0) - F^{(1)}(\zeta_0)]}{F^{(1)}(\zeta_0)F^{(2)}(\zeta_0)} + \frac{2U_\infty^{(2)}}{F^{(2)}(\zeta_0)}\right]. \tag{2.74}$$

As discussed in § 2.4.1, (2.74) should not be used for large roughnesses.

2.5.3. *Determination of* $a^{(1)}$

We compute $a^{(1)}$ by imposing (Trowbridge & Madsen 1984*b*)

$$u_{*wc}a^{(1)} = 2\overline{\mathrm{e}^{-\mathrm{i}\omega t}\left|\frac{\tau_{b1}}{\rho} + \frac{\tau_{b2}}{\rho}\right|^{1/2}}. \tag{2.75}$$

This yields (Trowbridge & Madsen 1984*b*)

$$2a^{(1)} = \frac{\overline{\tau}_b}{\tau_b^{(1)*}} + \frac{\overline{\tau}_b^*}{\tau_b^{(1)*}} + \frac{\tau_b^{(2)}}{\tau_b^{(1)}} - \frac{3}{5}\frac{\tau_b^{(2)*}}{\tau_b^{(1)*}}\frac{\tau_b^{(1)}}{\tau_b^{(1)*}}. \tag{2.76}$$

Substituting (2.50), (2.54) and (2.73) into (2.76) and using that $\overline{\tau}_b^* = \overline{\tau}_b$, we obtain

$$a^{(1)} = 2\frac{\overline{\tau}_b/\rho}{\kappa u_{*wc}U_\infty^{(1)*}/F^{(1)*}(\zeta_0)} + \frac{1}{4}\frac{a^{(1)}U_\infty^{(1)}[2/F^{(1)}(\zeta_0) - 1/F^{(2)}(\zeta_0)] + 2U_\infty^{(2)}/F^{(2)}(\zeta_0)}{U_\infty^{(1)}/F^{(1)}(\zeta_0)}$$
$$- \frac{3}{20}\frac{a^{(1)*}U_\infty^{(1)*}[2/F^{(1)*}(\zeta_0) - 1/F^{(2)*}(\zeta_0)] + 2U_\infty^{(2)*}/F^{(2)*}(\zeta_0)}{\left[U_\infty^{(1)*}/F^{(1)*}(\zeta_0)\right]^2}\frac{U_\infty^{(1)}}{F^{(1)}(\zeta_0)}. \tag{2.77}$$

This is an expression of the form

$$Aa^{(1)} + Ba^{(1)*} = C, \tag{2.78}$$

where the values of the complex constants A, B and C are given below. To solve, we write $a^{(1)} = a_\mathrm{r} + \mathrm{i}a_\mathrm{i}$, where the subindices r and i denote the real and imaginary parts, respectively. The complex constants A, B and C are decomposed into their real and imaginary parts analogously. This yields a linear system for the two unknowns (a_r and a_i), the solution of which is

$$a_\mathrm{r} = \frac{(A_\mathrm{r} - B_\mathrm{r})C_\mathrm{r} - (-A_\mathrm{i} + B_\mathrm{i})C_\mathrm{i}}{\Delta}, \tag{2.79}$$

$$a_\mathrm{i} = \frac{(A_\mathrm{r} + B_\mathrm{r})C_\mathrm{i} - (A_\mathrm{i} + B_\mathrm{i})C_\mathrm{r}}{\Delta}, \tag{2.80}$$

where

$$\Delta = A_\mathrm{r}^2 - B_\mathrm{r}^2 + A_\mathrm{i}^2 - B_\mathrm{i}^2 \tag{2.81}$$

and

$$A = A_\mathrm{r} + \mathrm{i}A_\mathrm{i} = 1 + \frac{1}{2}\frac{F^{(1)}(\zeta_0)}{F^{(2)}(\zeta_0)}, \tag{2.82}$$

$$B = B_\mathrm{r} + \mathrm{i}B_\mathrm{i} = \frac{3}{10}\frac{U_\infty^{(1)}F^{(1)*}(\zeta_0)}{U_\infty^{(1)*}F^{(1)}(\zeta_0)}\left(2 - \frac{F^{(1)*}(\zeta_0)}{F^{(2)*}(\zeta_0)}\right), \tag{2.83}$$

$$C = C_\mathrm{r} + \mathrm{i}C_\mathrm{i} = \frac{\overline{\tau}_b}{\rho\kappa u_{*wc}}\frac{4F^{(1)*}(\zeta_0)}{U_\infty^{(1)*}} + \frac{F^{(1)}(\zeta_0)U_\infty^{(2)}}{U_\infty^{(1)}F^{(2)}(\zeta_0)} - \frac{3}{5}\left[\frac{F^{(1)*}(\zeta_0)}{U_\infty^{(1)*}}\right]^2\frac{U_\infty^{(1)}}{F^{(1)}(\zeta_0)}\frac{U_\infty^{(2)*}}{F^{(2)*}(\zeta_0)}. \tag{2.84}$$

Since C is a function of $\overline{\tau}_b$, the previous expressions must be evaluated iteratively: first assume $\overline{\tau}_b = 0$, then compute C and $a^{(1)}$, update $\overline{\tau}_b$ (which is calculated as detailed below), and iterate until convergence.

The unknown parameters to completely characterize the boundary-layer hydrodynamics are the boundary-layer thickness, δ_w, the mean bed shear stress, $\overline{\tau}_b$, and the mean longitudinal pressure gradient, $\overline{G}$. The determination of δ_w is discussed in the following section. The determination of $\overline{\tau}_b$ and $\overline{G}$ depends on the geometry and flux conditions imposed in the oscillating water tunnel. In §§ 3.1 and 3.2, we will discuss how to obtain the solution in two cases of interest: (i) pure waves and (ii) waves combined with a current.

2.6. *Boundary-layer thickness*

The boundary-layer thickness is given by

$$\delta_w \equiv Al, \tag{2.85}$$

where $l \equiv \kappa u_{*wc}/\omega$ and u_{*wc} is the wave-current shear velocity based on the time-averaged combined shear stress. The coefficient A is a function of the relative roughness, X, which is defined by

$$X \equiv A_{bm,1}/k_n, \tag{2.86}$$

where $A_{bm,1} = u_{bm,1}/\omega$ is the near-bed first-harmonic orbital amplitude.

In order to obtain an expression for A, we run a modified version of our hydrodynamic model, in which no external or wave-induced current is accounted for. In this modified, pure wave version, the eddy viscosity is characterized by (2.21) for $z \leqslant \delta_I$, with $u_{*wc} = u_{*w}$, while it is assumed to remain constant for $z > \delta_I$. Thus, in this modified model, *a priori* knowledge of the boundary-layer thickness, δ_w, is not required. We run this model for pure sinusoidal waves with different values of the parameter X. For each run, we compute the amplitude of the first-harmonic wave velocity over the water column. The boundary-layer thickness, δ_w, is defined as the highest elevation above the bottom, where the maximum first-harmonic wave velocity differs from the potential flow velocity by more than 1 %, as illustrated in figure 3. Other values of this threshold (3 %, 5 %) have been explored. A threshold of 5 % is inadequate because for certain values of the roughness the maximum positive difference between the maximum first-harmonic wave velocity and the free-stream velocity becomes smaller than the threshold. A threshold of 3 % is a valid choice, which would alter the model predictions. Specifically, it would improve the agreement between predicted and inferred eddy viscosities in figure 7 below, but it would worsen the agreement between predicted and measured wave-current velocity profiles in figure 11 below.

The results of the boundary-layer thickness computations for the chosen 1 % threshold are shown in figure 4, which also displays a fitted approximation to the results. The maximum relative error of the fitted approximation is 0.9 %, and the computed and fitted curves are almost indistinguishable in figure 4. The fitting is

$$A = \begin{cases} \exp\{0.149X^{-0.37} + 1.69\}, & 0.02 \leqslant X \leqslant 0.1, \\ \exp\{1.99X^{-0.056} - 0.224\}, & 0.1 < X \leqslant 100, \\ \exp\{1.22X^{-0.10} + 0.538\}, & 100 < X \leqslant 10^5. \end{cases} \tag{2.87}$$

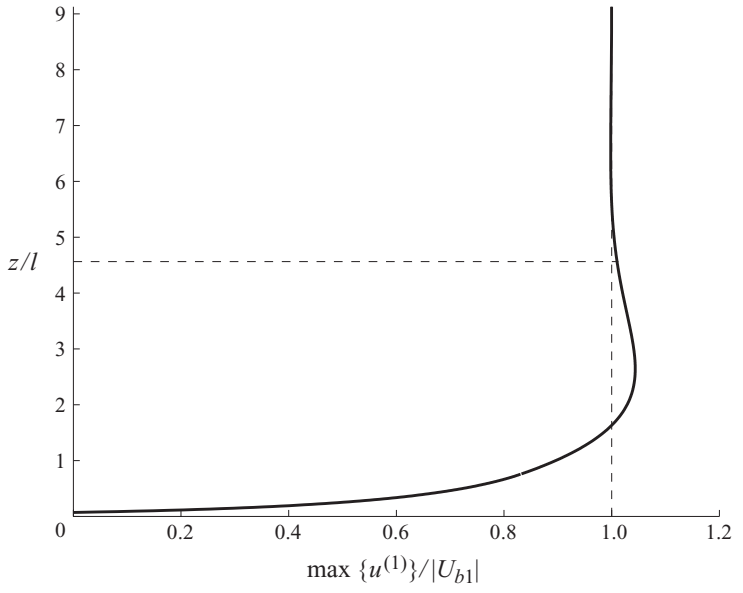

FIGURE 3. Computation of the boundary-layer thickness for $X = 10$. The thick solid line represents the maximum of the first harmonic of the velocity. The vertical dashed line indicates the free-stream velocity magnitude. The horizontal dashed line indicates the boundary-layer thickness, defined as the highest level above the bottom at which the maximum velocity departs by 1 % from the free-stream velocity. In the case represented in the figure, the result is $A = 4.57$.

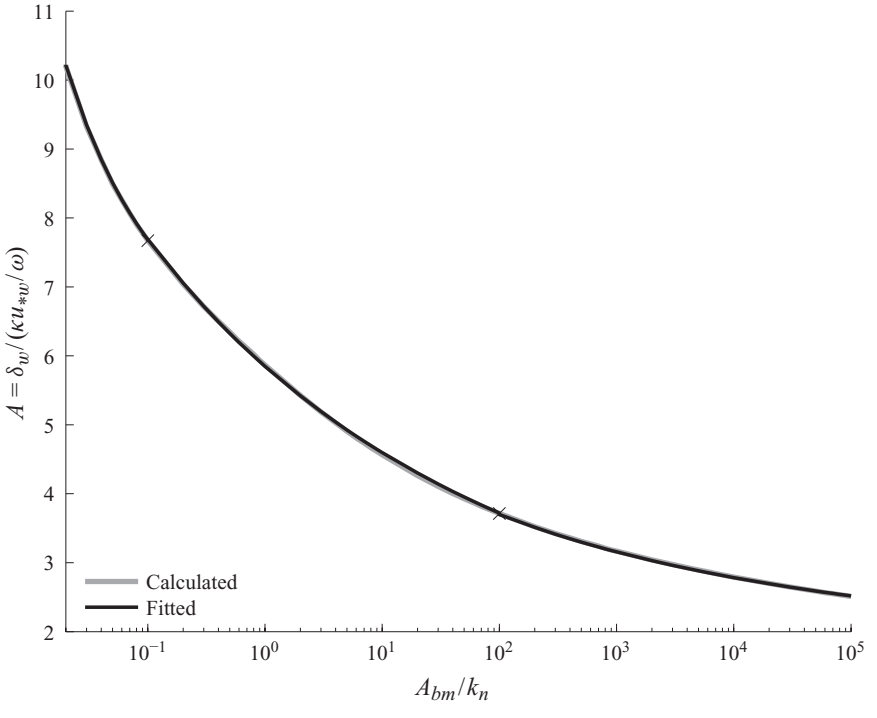

FIGURE 4. Calculated (grey line) versus fitted (black line) values of the boundary-layer thickness parameter, A, for different values of the relative roughness. The crosses indicate the boundaries between the three regions of the piecewise fitting, (2.87).

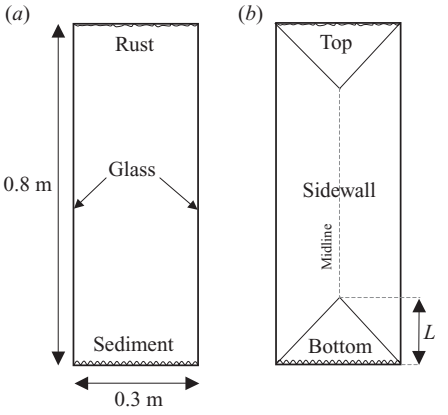

FIGURE 5. (*a*) Schematic of the working cross-section of the Delft oscillating water tunnel. (*b*) Schematic of the regions of influence of each boundary.

If the computation of the first-harmonic velocity were based on a constant (instead of a time-varying) eddy viscosity, the calculated values of A would differ by at most 6 % from those shown in figure 4.

3. Cross-sectional hydrodynamics of a tall narrow oscillating water tunnel

After having developed an analytical solution for the boundary layers, we now address the complete characterization of the whole cross-sectional hydrodynamics. Typical oscillating water tunnel sections are tall and narrow. For example, the working section of the Delft Hydraulics (Deltares) oscillating water tunnel is $b = 0.3$ m wide and $h = 0.8$ m tall, as illustrated in figure 5. For this geometry, the flow in most of the cross-section is governed by sidewall boundary-layer effects. In § 3, we will give detail about how to compute the velocities in the cross-section of a tall and narrow oscillating water tunnel for two cases: (i) pure waves and (ii) waves plus a current.

In an oscillating water tunnel, when the simulated near-bed wave orbital velocity is non-sinusoidal, a second-order mean velocity arises from the interaction between the time-dependent eddy viscosity and the time-dependent velocity, as reflected by the first term in (2.67), even with no current prescribed. This mean velocity yields a net flux. Since in the absence of a prescribed current the net cross-sectional flux is zero, a mean pressure gradient along the oscillating water tunnel is required to balance this local flux. Therefore, $\overline{G} \equiv \mathrm{d}\overline{p}/\mathrm{d}x \neq 0$, even when no mean current is imposed. The mean pressure gradient and the mean shear stresses are determined from continuity and total flux considerations, as explained in what follows.

3.1. *Pure waves*

In a tall and narrow oscillating water tunnel, most of the cross-sectional hydrodynamics are governed by the sidewall boundary layers, which should therefore be the starting point of the analysis. Since the wave-induced current is initially unknown, we first assume a value of u_{*c}/u_{*wc} (e.g. 0.1). The spatial structure of the eddy viscosity is given by (2.21), with $\delta_c = b/2$. We obtain the mean velocity and mean bed shear stress by using (2.57), (2.58), (2.66), (2.67), (2.79) and (2.80). Since the sidewalls are smooth, ζ_0 is determined from (2.62) with the value of α corresponding to smooth turbulent flow. There are two unknowns in these equations, the mean sidewall shear stress, $\overline{\tau}_{sw}$ (referred to as $\overline{\tau}_b$ in the equations), and the mean pressure

gradient, $\overline{G}$, which are determined by imposing

$$\left.\frac{\partial \overline{u}}{\partial z}\right|_{z=b/2} = 0, \tag{3.1}$$

$$2\int_{z_0}^{b/2} \overline{u}(z')\,\mathrm{d}z' = q_{sw}, \tag{3.2}$$

where z is the distance from the boundary (the sidewall) and q_{sw} is the volume flux per unit height of sidewall; q_{sw} is unknown, and it can be initially assumed to be zero. Equation (3.1) yields

$$\overline{\tau}_{sw} \approx -\left(\frac{b}{2} - z_0\right)\overline{G} \approx -\frac{b}{2}\overline{G}. \tag{3.3}$$

Then $\overline{G}$, the mean pressure gradient, is determined from (3.2) to be

$$\frac{\overline{G}}{\rho} = \frac{q_{sw} + C_1}{C_2}, \tag{3.4}$$

where

$$\begin{aligned} C_1 = {} & \frac{1}{\kappa u_{*wc}}\left[\frac{(\delta_I - z_0)^2}{2} + (b - \delta_I)(\delta_I - z_0) - \frac{b^2}{4}\ln\frac{\delta_I}{z_0}\right] \\ & + \frac{1}{\kappa u_{*wc}\delta_I}\left[\frac{\delta_J^2 - \delta_I^2}{2} - \frac{b}{2}(\delta_J - \delta_I)\right]\left(\frac{b}{2} - \delta_J\right) \\ & + \frac{1}{\kappa u_{*c}}\left[-\frac{\delta_K^2 - \delta_J^2}{2} + b(\delta_K - \delta_J) - \frac{b^2}{4}\ln\frac{\delta_K}{\delta_J}\right] \\ & + \frac{1}{\kappa u_{*c}\delta_L}\left[-\frac{b^3}{24} + \frac{b^2\delta_K}{4} - \frac{b\delta_K^2}{2} + \frac{\delta_K^3}{3}\right], \end{aligned} \tag{3.5}$$

$$\begin{aligned} C_2 = \mathrm{Re}\left\{\frac{a^{(1)*}}{2}U_\infty^{(1)}\left[\left(\frac{b}{2} - z_0\right) + \frac{\mathrm{i}}{F^{(1)}(\zeta_0)}\left(\frac{l}{2} + \left(\delta_I - \frac{u_{*c}}{u_{*wc}}\delta_J\right)\left.\frac{\mathrm{d}F^{(1)}}{\mathrm{d}\zeta}\right|_{\zeta=\delta_J/l}\right.\right.\right. \\ \left.\left.\left. + \frac{u_{*c}}{u_{*wc}}(\delta_K - \delta_L)\left.\frac{\mathrm{d}F^{(1)}}{\mathrm{d}\zeta}\right|_{\zeta=\delta_K/l}\right)\right]\right\}. \end{aligned} \tag{3.6}$$

Then, u_{*c} is determined from

$$u_{*c} = \sqrt{\frac{|\overline{\tau}_{sw}|}{\rho}}, \tag{3.7}$$

and this result is used to update the value of u_{*c}/u_{*wc}. This procedure is repeated iteratively. Upon convergence, the mean pressure gradient, $\overline{G}$, the midline mean eddy viscosity, $\overline{\nu}(z = b/2) = \overline{\nu}_{ml}$, and the midline mean velocity, $\overline{u}(z = b/2) = \overline{u}_{ml}$, are determined and can be used to compute the bottom boundary-layer flow.

Next, the bottom boundary layer is considered. The solution procedure is similar to the sidewall boundary layer. The values of u_{*c} and u_{*wc} in the bottom boundary layer are in general different from those in the sidewall boundary layer. Thus, we again need to assume a value of u_{*c}/u_{*wc}, solve the hydrodynamics, update the value of u_{*c}/u_{*wc} and iterate. The spatial structure of the eddy viscosity is again given by (2.21), where δ_L is now chosen so that the value of $\overline{\nu}$ in the midline is the same as that obtained from the sidewall analysis. If the bottom is rough, the value of ζ_0 must

be determined using (2.63). The two remaining unknowns are the mean bottom shear stress, $\overline{\tau}_b$, and the distance from the bottom, L, at which the mean velocity, $\overline{u}$, matches the midline velocity, $\overline{u}_{ml}$ (see figure 5). These unknowns are determined by imposing

$$\left.\frac{\partial \overline{u}}{\partial z}\right|_{z=L} = 0, \tag{3.8}$$

$$\overline{u}(z = L) = \overline{u}_{ml}. \tag{3.9}$$

Equation (3.8) results in

$$\overline{\tau}_b \approx -(L - z_0)\,\overline{G} \approx -L\overline{G}. \tag{3.10}$$

Combining this with (3.9) results in a quadratic equation for L whose solution is

$$L = \frac{-b + \sqrt{b^2 - 4ac}}{2a}, \tag{3.11}$$

where

$$a = \frac{1}{2u_{*c}\delta_L}, \tag{3.12}$$

$$b = \frac{1}{u_{*wc}} \ln\frac{\delta_I}{z_0} + \frac{\delta_J - \delta_I}{u_{*wc}\delta_I} + \frac{1}{u_{*c}} \ln\frac{\delta_K}{\delta_J} - \frac{\delta_K}{u_{*c}\delta_L}, \tag{3.13}$$

$$c = \frac{\kappa}{\overline{G}/\rho}\left[\overline{u}_{ml} + \mathrm{Re}\left\{\frac{a^{(1)*}}{2}U_\infty^{(1)}\right\}\right] - \frac{\delta_I - z_0}{u_{*wc}} - \frac{\delta_J^2 - \delta_I^2}{2u_{*wc}\delta_I} - \frac{\delta_K - \delta_J}{u_{*c}} + \frac{\delta_K^2}{2u_{*c}\delta_L}. \tag{3.14}$$

With the mean bed shear stress determined from (3.10), the current shear velocity is updated using

$$u_{*c} = \sqrt{\frac{|\overline{\tau}_b|}{\rho}}, \tag{3.15}$$

and the value of u_{*c}/u_{*wc} is updated accordingly. The process is repeated until convergence.

Then, the top boundary layer is solved in exactly the same manner as the bottom boundary layer, with the appropriate choice of α in (2.63) depending on whether the top is rough or smooth.

Once the mean velocities in the three boundary layers (sidewall, bottom and top) have been computed, the total mean flow through the whole cross-section is calculated. In the calculations presented in § 4, this is done in the following manner. The section is split into regions governed by the sidewalls, top and bottom, by matching the velocities at points located at a distance $b/4$ and $b/2$ from the sidewalls (P, Q, R and S in figure 6). For example, the location of point P is determined by imposing that the mean velocities of the sidewall and bottom boundary layers match at P. In this way, the net cross-sectional flux is determined. Then, the old value of q_{sw} is corrected to yield a zero net flux, and the whole analysis is repeated with the new value of q_{sw}. Convergence is usually attained after few iterations.

3.2. *Waves plus a current*

Next, we consider the case of a mean flow imposed in addition to the oscillatory motion. If a total cross-sectional mean flux is prescribed, the solution procedure is identical to the one described in § 3.1, except that now the prescribed non-zero mean flux is imposed when updating the value of q_{sw}. On the other hand, if the mean flow is prescribed by means of a reference current velocity (u_{ref}) at a certain elevation above the bottom ($z = z_{ref}$), the solution procedure becomes simpler, as there is no

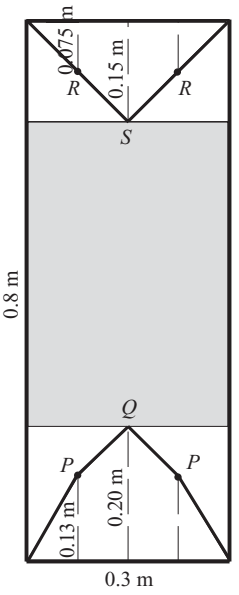

FIGURE 6. Split of the oscillating water tunnel cross-section between areas of influence of the sidewall, top and bottom boundary layers (thick solid lines), by matching velocities at points P, Q, R and S. The shaded area corresponds to the main sidewall region, with a flux per unit height of q_{sw}. The specific dimensions indicated in the figure correspond to application of our model to test 1 reported by Ribberink & Al-Salem (1995), assuming the top boundary to be smooth.

need to iterate to match a prescribed value of the total flux. The solution procedure for this latter case is as follows. First, we solve for the sidewall boundary layer, in which the two unknowns, $\overline{\tau}_{sw}$ and $\overline{G}$, are determined by imposing

$$\left.\frac{\partial \overline{u}}{\partial z}\right|_{z=b/2} = 0, \tag{3.16}$$

$$\overline{u}(b/2) = u_{ref}. \tag{3.17}$$

Equation (3.16) results in

$$\overline{\tau}_{sw} \approx -\frac{b}{2}\overline{G}, \tag{3.18}$$

which, upon substitution into (3.17), yields

$$\begin{aligned}\frac{\overline{G}}{\rho} = &\left\{\kappa\left[u_{ref} + \mathrm{Re}\left(\frac{a^{(1)*}}{2}U_\infty^{(1)}\right)\right]\right\}\left\{\frac{1}{u_{*wc}}\left[(\delta_I - z_0) - \frac{b}{2}\ln\frac{\delta_I}{z_0}\right]\right.\\ &+ \frac{1}{u_{*wc}\delta_I}\left[\frac{\delta_J^2 - \delta_I^2}{2} - \frac{b}{2}(\delta_J - \delta_I)\right] + \frac{1}{u_{*c}}\left[(\delta_K - \delta_J) - \frac{b}{2}\ln\frac{\delta_K}{\delta_J}\right]\\ &\left.+ \frac{1}{u_{*c}\delta_L}\left[\frac{(b/2)^2 - \delta_K^2}{2} - \frac{b}{2}\left(\frac{b}{2} - \delta_K\right)\right]\right\}^{-1}.\end{aligned} \tag{3.19}$$

With $\overline{G}$ known, we then solve the bottom boundary layer. The only unknown, $\overline{\tau}_b$, is determined by imposing

$$\overline{u}\left(z_{ref}\right) = u_{ref}. \tag{3.20}$$

If $z_{ref} \geqslant \delta_K$, (3.20) yields the following equation for $\overline{\tau}_b$:

$$\frac{\overline{\tau}_b}{\rho} = \left\{\kappa u_{ref} + \kappa \mathrm{Re}\left[\frac{a^{(1)*}}{2} U_\infty^{(1)}\right] - \frac{\overline{G}}{\rho}\left[\frac{1}{u_{*wc}}\left((\delta_I - z_0) - z_0 \ln\frac{\delta_I}{z_0} + \frac{\delta_J^2 - \delta_I^2}{2\delta_I} - z_0\frac{\delta_J - \delta_I}{\delta_I}\right)\right.\right.$$
$$\left.\left. + \frac{1}{u_{*c}}\left((\delta_K - \delta_J) - z_0 \ln\frac{\delta_K}{\delta_J} + \frac{z_{ref}^2 - \delta_K^2}{2\delta_L} - z_0\frac{z_{ref} - \delta_K}{\delta_L}\right)\right]\right\}$$
$$\left\{\frac{1}{u_{*wc}}\left[\ln\frac{\delta_I}{z_0} + \frac{\delta_J - \delta_I}{\delta_I}\right] + \frac{1}{u_{*c}}\left[\ln\frac{\delta_K}{\delta_J} + \frac{z_{ref} - \delta_K}{\delta_L}\right]\right\}^{-1}. \tag{3.21}$$

4. Comparison with hydrodynamic measurements in an oscillating water tunnel

In § 4, we test the ability of our hydrodynamic model to predict experimental measurements from oscillating water tunnels for pure sinusoidal waves, pure skewed waves and waves combined with a current. These comparisons demonstrate the need to use a time-varying eddy viscosity to correctly capture the hydrodynamics. It is noted that our hydrodynamic model does not include any calibration parameter that is fitted using the experimental data.

4.1. *Sinusoidal waves*

To validate the analytical boundary-layer model, we first compare its near-bed hydrodynamic predictions with oscillating water tunnel measurements for sinusoidal waves reported by Jonsson & Carlsen (1976). Trowbridge & Madsen (1984*a*) compared their model's predictions to the first- and third-harmonic velocity amplitudes and arguments measured by Jonsson and Carlsen; the model presented here has a comparable ability to reproduce these measurements (see Gonzalez-Rodriguez 2009, for details). The existence of the third harmonic cannot be captured by a constant eddy viscosity model, which underlines the relevance of modelling the eddy viscosity time dependence.

A more definite verification of our time-dependent eddy viscosity model is provided by the comparison between our assumed eddy viscosity and the values inferred from Jonsson & Carlsen's (1976) measurements. To estimate the eddy viscosity harmonics from the velocity measurements, we first estimate the experimental shear stresses by using the relationship

$$\frac{\tau_{zx}(z)}{\rho} = -\int_L^z \frac{\partial}{\partial t}(u_b - u(z'))\,\mathrm{d}z', \tag{4.1}$$

where L is the distance from the bottom at which the wave velocity becomes essentially constant and u_b is the wave velocity at that location. Equation (4.1) is obtained from vertical integration of the boundary-layer equation between z and L. In terms of Fourier harmonics

$$\frac{\tau^{(k)}}{\rho} = -\int_L^z k\mathrm{i}\omega\left(u_b^{(k)} - u^{(k)}(z)\right)\mathrm{d}z, \tag{4.2}$$

where $k = 1, 2, 3$ indicate the different harmonics and $u^{(k)}(z)$ are obtained from Fourier analysis of the velocities measured at different elevations above the bed. Next, by using the expressions for the first and third harmonic bed shear stresses, (2.48) and (2.53), we obtain the following estimates of the mean and second-harmonic eddy

viscosity components:

$$\overline{\nu} = \left[\frac{\tau^{(1)}}{\rho}\frac{\mathrm{d}u^{(1)}}{\mathrm{d}z} - \frac{\tau^{(3)}}{\rho}\frac{\mathrm{d}u^{(1)*}}{\mathrm{d}z}\right]\left[\frac{\mathrm{d}u^{(1)}}{\mathrm{d}z}\frac{\mathrm{d}u^{(1)}}{\mathrm{d}z} - \frac{\mathrm{d}u^{(3)}}{\mathrm{d}z}\frac{\mathrm{d}u^{(1)*}}{\mathrm{d}z}\right]^{-1}, \tag{4.3}$$

$$a^{(2)} = \frac{2}{\mathrm{d}u^{(1)*}/\mathrm{d}z}\left[\frac{1}{\overline{\nu}}\frac{\tau^{(1)}}{\rho} - \frac{\mathrm{d}u^{(1)}}{\mathrm{d}z}\right]. \tag{4.4}$$

Using (2.73), the following estimate for the relative magnitude of the first-harmonic eddy viscosity is obtained:

$$a^{(1)} = \frac{2}{\mathrm{d}u^{(1)*}/\mathrm{d}z}\left[\frac{1}{\overline{\nu}}\frac{\tau^{(2)}}{\rho} - \frac{\mathrm{d}u^{(2)}}{\mathrm{d}z}\right]. \tag{4.5}$$

It is noted that both the numerators and denominators of (4.3)–(4.5) become very small as $z \to L$. Therefore, the eddy viscosity values inferred from measurements in the upper region of the boundary layer contain large errors and should be disregarded.

Figure 7 shows comparisons of the estimated and inferred eddy viscosity harmonics for Jonsson and Carlsen's tests 1 (a, b) and 2 (c, d). As shown in figures 7(a) and 7(c), the model's assumed mean eddy viscosity is in reasonable agreement with the inferred values, especially in the most crucial region closest to the bottom. Figures 7(b) and 7(d) show the existence of a second harmonic of the eddy viscosity of magnitude and structure comparable to those assumed by the model, thus confirming our use of a time-varying eddy viscosity. As seen in figure 7(b,d), a first-harmonic eddy viscosity, not expected for pure waves, is also inferred from the measurements. The inferred first-harmonic eddy viscosity for test 1 is much smaller than the second harmonic and can be attributed to measurement errors. For test 2, however, the inferred first- and second-harmonic eddy viscosities are of comparable magnitude. As discussed by Trowbridge (1983), the (very small) second-harmonic velocity measurements of test 2 lack any vertical structure and appear dominated by noise, explaining why, for this case, a meaningless first-harmonic eddy viscosity is obtained. Plots (a) and (c) suggest that the model's wave boundary-layer thickness estimate, based on the 99 percentile of the free-stream velocity (see § 2.6), is overpredicted. A reduction of this percentile would, however, worsen the agreement with the inferred second-harmonic eddy viscosity in plots (b) and (d), since the second harmonic would then vary linearly over a longer distance than predicted.

4.2. *Pure skewed waves*

Here we compare the hydrodynamic results of our model with measurements by Ribberink & Al-Salem (1995). These experiments were conducted in the Delft oscillating water tunnel, which has a cross-section of width $b = 0.3$ m and total height of 1.1 m. During the experiments, the bottom 30 cm were filled with sand, so that the height of the flow cross-section was $h = 0.8$ m. Measurements of cross-sectional velocities and of sediment transport rates were recorded. Here we focus on the former. Three cases were considered in the experiment. In one case waves were sinusoidal, and no streaming was observed. This is consistent with our theory, in which a second harmonic of the velocity is necessary to yield a first harmonic of the eddy viscosity and thus streaming. In the other two cases, referred to as test 1 and test 2, the waves were second-order Stokes (i.e. skewed but symmetric). The wave and sediment characteristics are summarized in table 1. In these cases, a mean streaming was observed. In this section we compare the instantaneous and mean (streaming) velocities predicted by our model with the measurements.

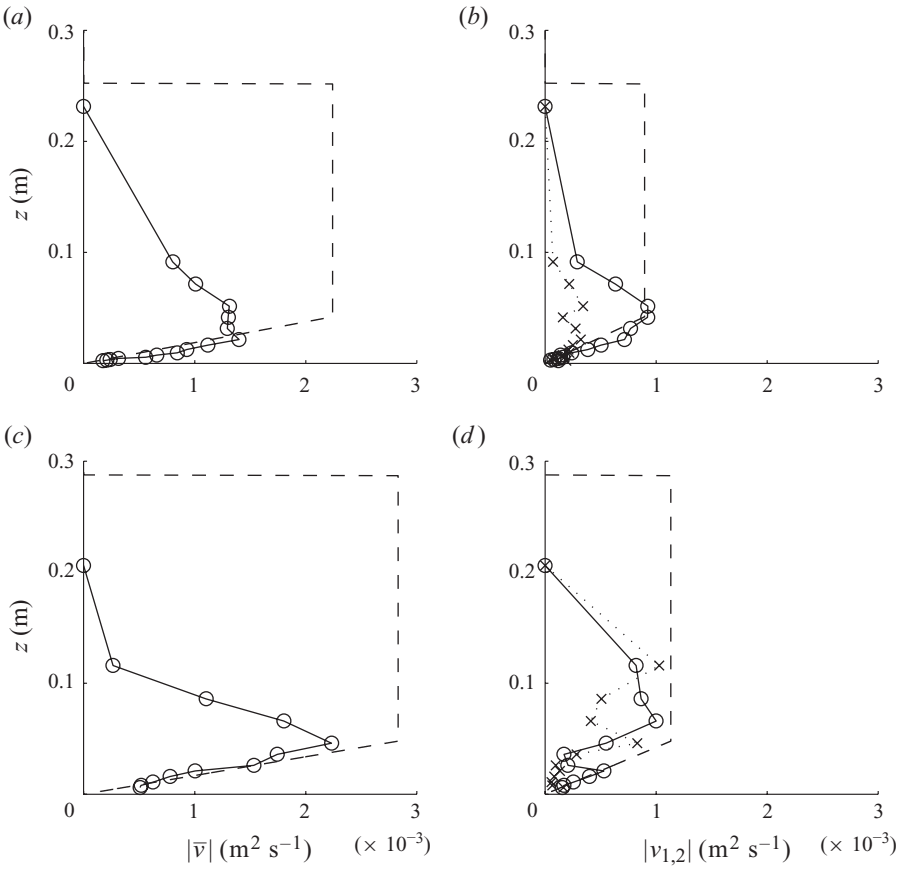

FIGURE 7. Comparison between predicted eddy viscosities and values inferred from Jonsson & Carlsen's (1976) measurements for test 1 (plots (*a*) and (*b*)) and test 2 (plots (*c*) and (*d*)). (*a*, *c*) Predicted (dashed line) and inferred (solid line with circle markers) mean absolute eddy viscosity velocity amplitudes. (*b*, *d*) Predicted second harmonic (dashed line), inferred second harmonic (solid line with circle markers) and inferred first harmonic (dotted line with cross markers).

Since the cross-section of the oscillating water tunnel is tall and narrow, we expect the flow in most of the cross-section to be governed by the sidewall boundary layers. This corresponds to the case of pure waves in a narrow oscillating water tunnel discussed in § 3.1. Applying our model as discussed in that section, we predict instantaneous and mean velocities, which we can compare with the measurements. Since the bottom is covered with movable sediment, the hydraulic bed roughness is estimated using Herrmann & Madsen's (2007) formula

$$k_n = [4.5\,(\Psi - \Psi_{cr}) + 1.7]\,D_n, \tag{4.6}$$

where Ψ is the Shields parameter

$$\Psi = \frac{\tau_m}{(\rho_s - \rho)\,g\,D_{50}}, \tag{4.7}$$

Ψ_{cr} is the critical Shields parameter for initiation of motion, D_n is the nominal diameter ($D_n \approx 1.1 D_{50}$), τ_m is the maximum bed shear stress and ρ_s is the density of

Case	$U_\infty^{(1)}$ (m s^{-1})	$U_\infty^{(2)}$ (m s^{-1})	T (s)	D_{50} (mm)
Test 1	0.8082	0.2586	6.5	0.21
Test 2	0.8171	0.2288	9.1	0.21

TABLE 1. Experimental conditions for the skewed wave cases reported by Ribberink & Al-Salem (1995).

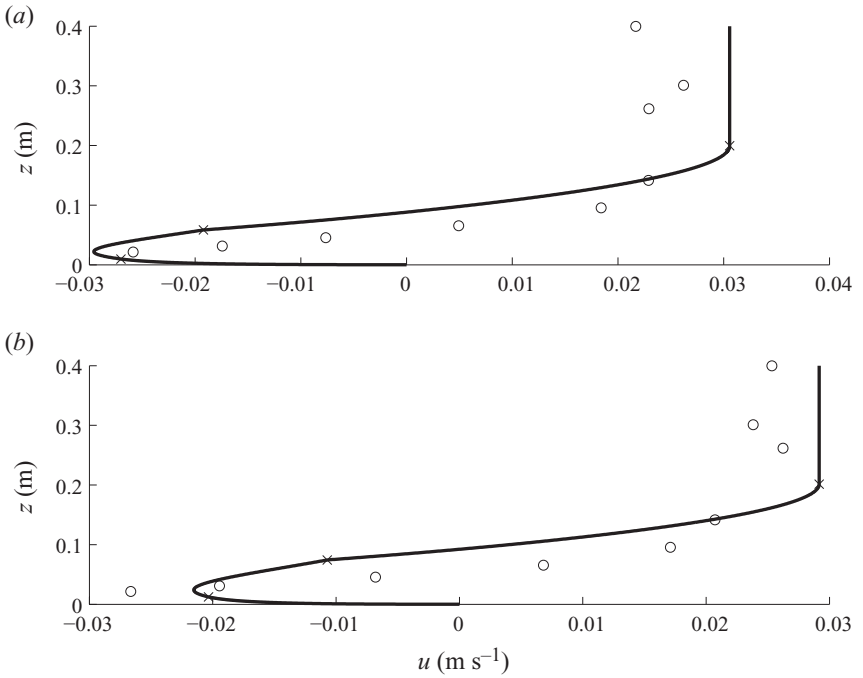

FIGURE 8. Predicted (solid line) and measured (circles, Ribberink & Al-Salem 1995) mean velocities for (*a*) test 1 and (*b*) test 2. The crosses indicate the boundaries between the different regions of the piecewise eddy viscosity. The oscillating water tunnel's ceiling is assumed to be smooth ($k_n = 0$ at the top).

the sediment ($\rho_s \approx 2650\,\mathrm{kg\,m^{-3}}$ for quartz). Due to its dependence on the maximum bed shear stress, the mobile-bed roughness must be determined iteratively.

Figure 8 shows a comparison between the predicted and measured mean velocities for tests 1 and 2, assuming the ceiling of the oscillating water tunnel to be smooth ($k_n = 0$). The predicted near-bed mean velocities are insensitive to this assumption, and almost indistinguishable values are obtained even if the ceiling is assumed very rough (Gonzalez-Rodriguez 2009). The large velocity under the crest of a second-order Stokes wave is taken to be positive, and we shall refer to positive velocities as onshore. The model correctly predicts negative mean velocities in the region closest to the boundary, and positive velocities above. The negative velocities near the boundary are induced by the interaction between the first harmonics of the eddy viscosity and the velocity, as shown by (2.67), and the positive velocities farther above the boundary are a consequence of conservation of total mass in the tunnel. The magnitudes of the maximum positive and negative velocities, of about 3 cm s^{-1}, are also correctly reproduced by the model. However, the height of the region of negative velocities is

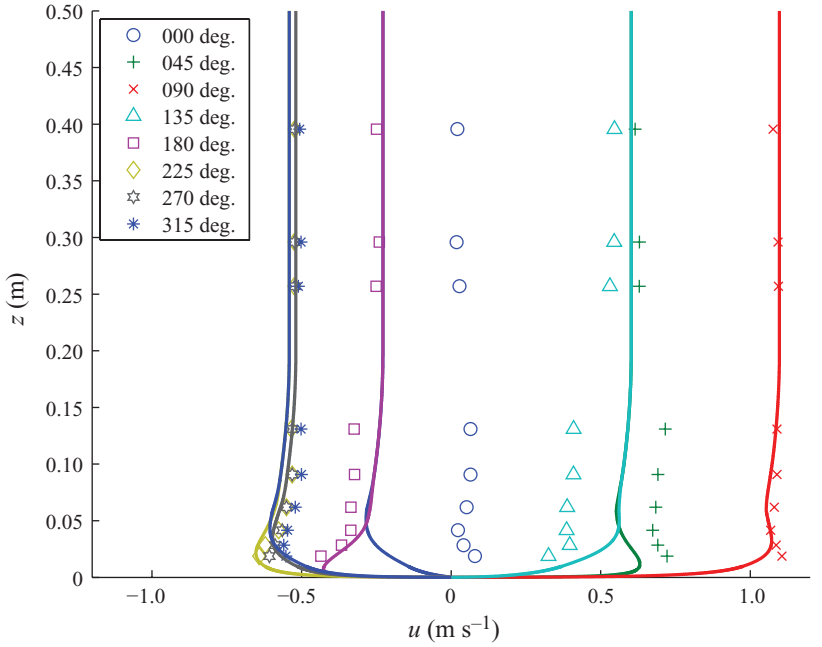

FIGURE 9. Predicted (solid lines) and measured (symbols, Ribberink & Al-Salem 1995) instantaneous near-bed velocities for test 1. The oscillating water tunnel's ceiling is assumed to be smooth ($k_n = 0$ at the top).

slightly overpredicted by the model. The predictions shown in the figure correspond to our definition of the boundary-layer thickness based on a 1 % departure from the free-stream velocity. A better agreement can be obtained by defining the boundary-layer thickness using a larger percentage. The crosses in figure 8 indicate the boundaries between the different regions of the piecewise eddy viscosity. For the bottom boundary layer in tests 1 and 2, the current is so weak that $\delta_{wc} > \delta_w$, and therefore the third region of the piecewise eddy viscosity defined by (2.21) does not exist. As a result, there is a jump in the eddy viscosity value at $z = \delta_w \approx 6$ cm, which produces a kink in the velocity profile, most apparent in figure 8(*b*).

Figure 9 shows the predicted and measured instantaneous velocities along the midline of the oscillating water tunnel and near the bottom boundary. The colours of the solid lines (predictions) and symbols (measurements) correspond to different phases over the wave period. As shown in the figure, the thickness of the boundary layer (identifiable by the overshoot in the velocity profile) is well predicted by the model. The agreement between predictions and measurements is good near the wave crest (phase of $\approx 90°$) and trough (phase of $\approx 270°$) and bad near the zero up-crossing (phase of $\approx 0°$). The reason for this lack of agreement is that the measured free-stream velocity near the zero up-crossing significantly diverges from the Stokes second-order free-stream velocity intended in the experiment. This intended free-stream velocity was used as a model input, and corresponds to the asymptotic value of the predicted instantaneous velocity at the upper edge of the boundary layer. The lack of agreement between intended and measured free-stream velocities is shown in figure 10, where the solid line indicates the experimentally intended free-stream velocity (used as the model input) and the symbols indicate the velocities measured at 40 cm above the boundary. The symbols used in figures 9 and 10 consistently

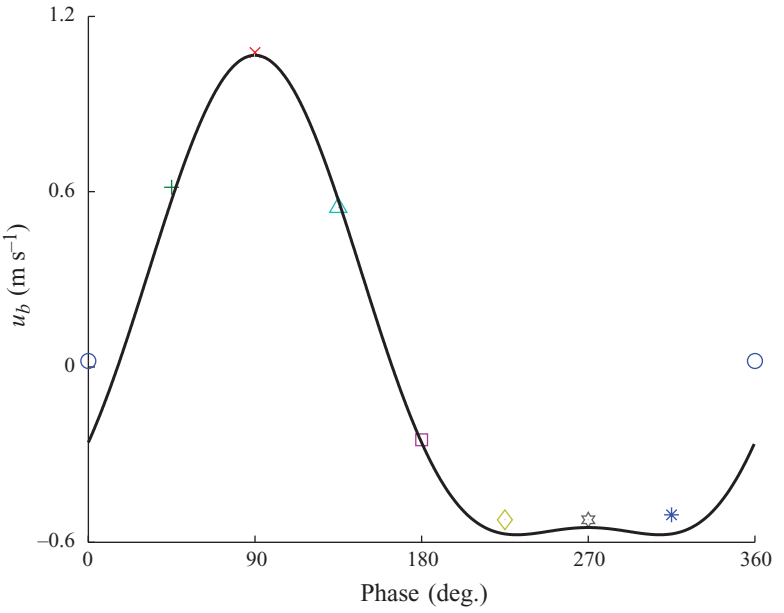

FIGURE 10. Intended (solid line) and measured (symbols, Ribberink & Al-Salem 1995) free-stream velocities at 4.0 cm above the bed for test 1.

correspond to the same phases, showing that the worst agreement between predicted and measured instantaneous velocities (circles, phase of 0°) correspond to the worst agreement between the intended and the actual free-stream velocities. At this phase, the intended free-stream velocity was −0.26 m s^{-1}, while the measured velocity was 0.02 m s^{-1}.

Predictions of streaming for the pure asymmetric wave conditions of van der A *et al.* (2008), presented by Gonzalez-Rodriguez (2009), do not match the reported measurements. For pure asymmetric waves, van der A *et al.* (2008) measured an offshore-directed near-bed streaming (i.e. streaming opposite to the direction of the largest near-bed wave acceleration), analogous to that observed by Ribberink & Al-Salem for pure skewed waves. In contrast, Fuhrman *et al.* (2009), who used a numerical model based on a k–ω turbulence closure, found an onshore streaming under asymmetric waves. However, it is noted that the streaming is a small magnitude that scales as the mean bed shear stress, which is shown to have a negligible effect on the sediment transport predictions. Bedload is proportional to the 3/2-power of the bed shear stress; therefore, even if the predicted mean bed shear stress due to an asymmetric wave is negative, the bedload can be directed onshore provided that the instantaneous maximum bed shear stress is sufficiently larger, in magnitude, than the instantaneous minimum bed shear stress. This is indeed what our model predicts for the asymmetric wave cases of van der A *et al.* (2010), where there is good agreement between predicted and measured bedload transport rates (see § 5) in spite of the streaming disagreement. In conclusion, lack of agreement between predictions of the streaming for asymmetric waves does not preclude good agreement for the corresponding sediment transport rates.

4.3. *Waves plus a current*

Next, we apply our model to cases of sinusoidal waves combined with a current reported by Dohmen-Janssen (1999). The experiments were performed in the Delft

Case	z_{ref} (m)	u_{ref} (m s^{-1})	u_{bm} (m s^{-1})	T (s)	D_{50} (mm)	bed condition	k_n (mm)
G5	0.10	0.45	0.95	7.2	0.21	Fixed	0.21
G6	0.10	0.45	1.50	7.2	0.21	Fixed	0.21
D1	0.10	0.24	1.47	7.2	0.13	Mobile	4.7
D2	0.10	0.24	1.47	7.2	0.21	Mobile	4.9
T1	0.10	0.25	1.10	4.0	0.13	Mobile	3.0
T2	0.10	0.25	1.10	12.0	0.13	Mobile	2.2

TABLE 2. Experimental conditions for wave-current cases reported by Dohmen-Janssen (1999) and roughnesses predicted by the analytical model.

oscillating water tunnel ($b = 0.3$ m, $h = 0.8$ m). The wave and sediment conditions of the series considered here are summarized in table 2. Our model is applied using the procedure described in § 3.2, with the current specified by its velocity, u_{ref}, measured at a reference elevation, z_{ref}, as indicated in table 2. For the fixed-bed cases (G5 and G6), the bed roughness is taken as the median sediment diameter, D_{50}; for the mobile-bed cases, the bed roughness is determined using Herrmann & Madsen's formula, (4.6), with Ψ in (4.7) based on the maximum combined wave-current shear stress. Comparisons of measured and predicted current profiles are shown in figure 11. It is noted that the good fit of these particular hydrodynamic predictions does not rely on the use of a time-varying eddy viscosity, since similar or even better wave-current velocity predictions can be obtained with a modified Grant & Madsen's (1979) wave-current model, based on a time-invariant eddy viscosity, as discussed by Gonzalez-Rodriguez (2009).

5. Bedload predictions and comparison with measurements

We apply the analytical boundary-layer model developed in § 2 to predict bedload in oscillating water tunnels. In analogy to Gonzalez-Rodriguez & Madsen (2007), we predict bedload transport by using Madsen's formula (Madsen 1991, 2002). According to Madsen's formula, the instantaneous bedload sediment transport rate in a two-dimensional flow is

$$q_{sb}(t) = \frac{8}{(s-1)\rho g} \max\left[0, |\tau_b(t)| - \tau_{cr,\beta}\right] \frac{\left(\sqrt{|\tau_b(t)|/\rho} - \alpha_\beta \sqrt{\tau_{cr,\beta}/\rho}\right)}{\cos\beta\,(\tan\phi_m + \tan\beta)} \frac{\tau_b(t)}{|\tau_b(t)|}, \tag{5.1}$$

where β is the bottom slope in the direction of transport, taken to be positive if sediment is transported upslope, $s = \rho_s/\rho$ is the ratio between sediment and fluid densities, $\tau_{cr,\beta}$ is the critical shear stress for initiation of motion, given by

$$\tau_{cr,\beta} = \tau_{cr,0}\left[\cos\beta\left(1 + \frac{\tan\beta}{\tan\phi_s}\right)\right], \tag{5.2}$$

where $\tau_{cr,0}$ is determined using the Shields diagram (e.g. Madsen 2002). The parameter α_β in (5.1) is given by

$$\alpha_\beta = \frac{\sqrt{\tan\phi_m + \tan\beta}}{\sqrt{\tan\phi_s + \tan\beta}}, \tag{5.3}$$

where $\phi_s \approx 50^\circ$ and $\phi_m \approx 30^\circ$ are the values of the angles of static and moving friction recommended by Madsen (2002). In applying (5.1), the bed shear stress, $\tau_b(t)$, is calculated using our boundary-layer model described above.

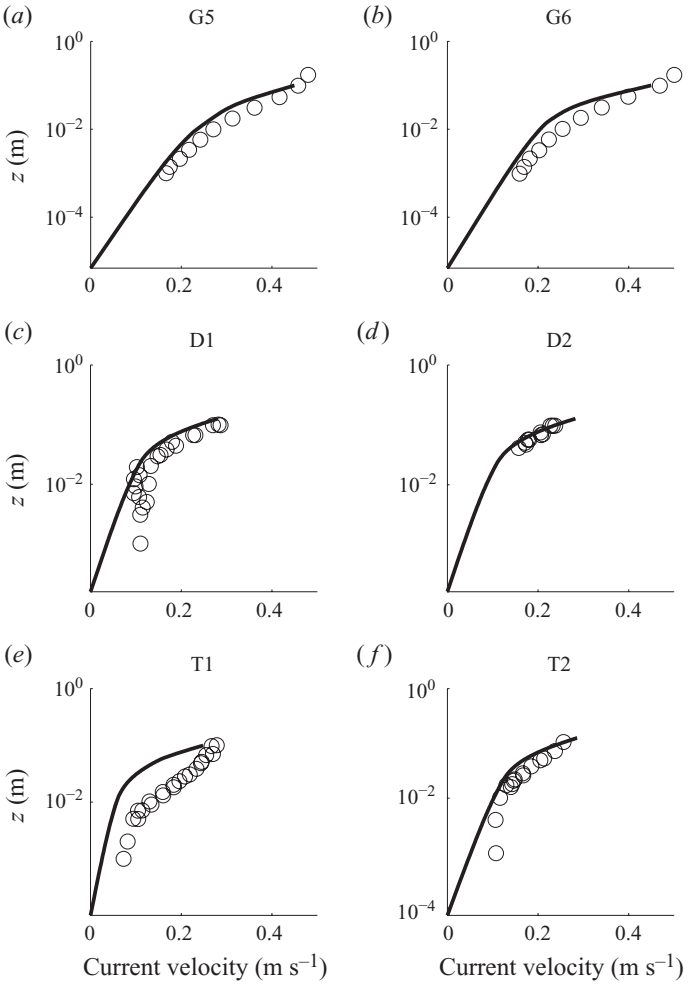

FIGURE 11. Measurements (circles) and predictions (solid line) for mean velocities near the bottom in series G, D and T reported by Dohmen-Janssen (1999).

The bedload experiments considered here correspond to sheet flow conditions. As discussed in § 1, the appropriate choice of sheet flow roughness to compute the effective bed shear stress for sediment transport remains an open question. Here, this effective roughness is taken equal to the total roughness and parametrized using Herrmann & Madsen's (2007) formula (4.6). As shown below, this parametrization consistently yields good results, suggesting that the effective roughness for sheet flow sediment transport is the total, mobile-bed roughness.

Madsen's formula (5.1) is only applicable when suspension effects are negligible, i.e. when the ratio of the maximum shear velocity (u_{*m}) to the sediment fall velocity (w_f) is smaller than a certain threshold value. By comparing bedload predictions based on $k_n = D_{50}$ with total sediment transport rate measurements, Gonzalez-Rodriguez & Madsen (2007) proposed a threshold value of $u_{*m}/w_f < 2.7$ for suspension effects to be negligible. Following the same procedure as Gonzalez-Rodriguez & Madsen (2007), we find that the threshold should be modified to $u_{*m}/w_f < 4$ when the bed shear stress is computed based on the total mobile-bed roughness (4.6), as will be

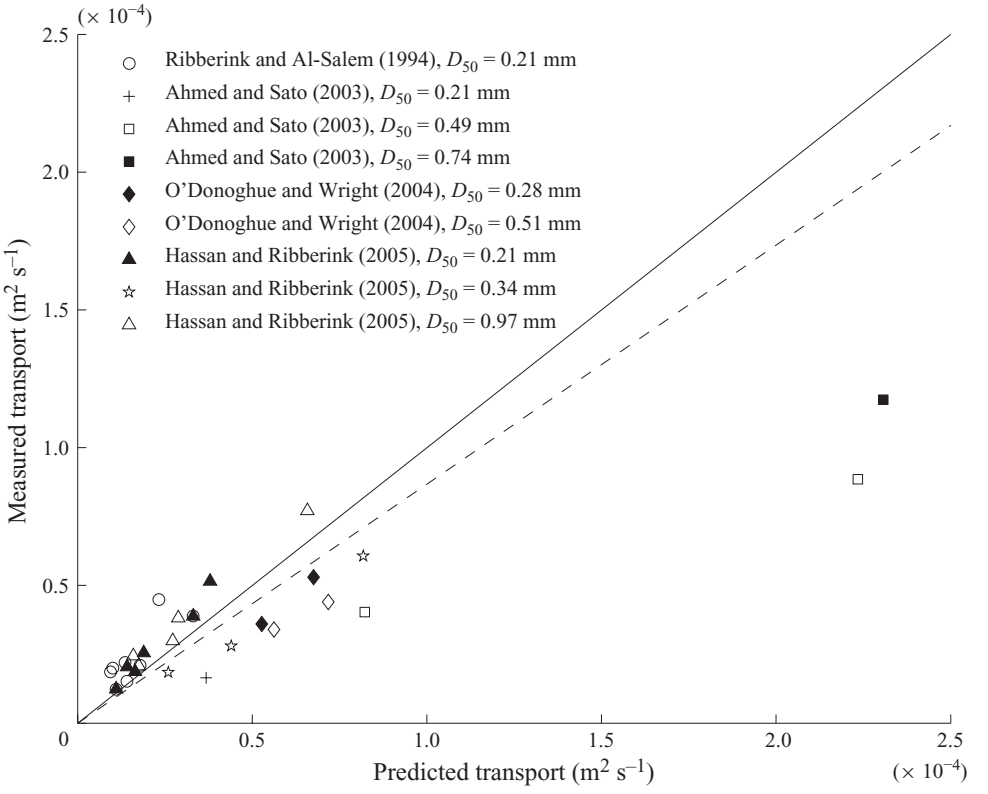

FIGURE 12. Comparison between measured and predicted average sediment transport rates under skewed, symmetric waves for bedload-dominated cases ($u_{*m}/w_s < 4$). Predictions are obtained using the analytic boundary-layer model with mobile-bed roughness. The solid line corresponds to perfect agreement between predictions and measurements, while the dashed line is the least-squares fit to the data (excluding the two data points with the largest transport rates) and corresponds to an overprediction by a factor of 1.2.

done here, and the sediment fall velocity is estimated using the formula of Jimenez & Madsen (2003).

When comparing predictions and measurements of net sediment transport rates, it must be emphasized that the net transport rate is the small difference between two large quantities, the onshore and offshore transport rates. Thus, small errors in the bed shear stress predictions yield large errors in the transport. For example, for one of the experimental cases considered below (Ahmed and Sato 2003, case 15), we have observed that a small error of 4 % in the bed shear stress predictions yields a 27 % error in the net sediment transport rate (Gonzalez-Rodriguez 2009). For this reason, surf zone sediment transport models can only provide rough estimates of the actual transport rates, and rather large errors are tolerated. For example, according to the Brier skill score (BSS) proposed by van Rijn *et al.* (2003) and applied by van der A *et al.* (2010), errors between net transport rates predictions and measurements of about 40, 60 and 80 % are considered as excellent, good and fair, respectively. As shown below, our model's predictions are accurate within a typical error of 20–60 %.

Figure 12 shows a comparison between the model's predictions and experimental sediment transport data sets of purely skewed waves in oscillating water tunnels

(Ribberink & Al-Salem 1994, series B, cases 7–16; Ahmed & Sato 2003, cases U1–U13 and U15; O'Donoghue & Wright 2004, series MA and CA; Hassan & Ribberink 2005, series R and Q). In the experiments, the near-bed orbital velocity is symmetric ($As = 0$), but skewed ($0.13 < Sk < 0.31$). The bed remained flat. All studies measured average transport rates over the entire wave cycle, with the exception of Hassan & Ribberink (2005, series Q), in which the onshore and offshore transport components over half-wave cycles were measured separately. Our model's predictions are based on the wave velocities inferred from the motion of the wave piston. For the cases of Ahmed & Sato (2003), we use the near-bed velocity time-series provided by the authors (A. S. M. Ahmed, personal communication, 2006). For all other cases, the near-bed velocities are modelled as second-order Stokes waves. The predicted bed shear stresses are based on the total mobile-bed roughness. Only bedload-dominated cases, for which the predicted $u_{*m}/w_s < 4$, are shown in the figure. The analytical model based on the mobile-bed roughness yields good bedload predictions for skewed waves, with slight overpredictions by a factor of 1.2 or less. The exceptions are two data points corresponding to large transport rates, for which the analytical model yields overpredictions by a factor of about 2. It is noted that the larger transport for these two data points is due to a larger value of the near-bed velocity, while their skewness value is comparable to that of other data points. These are therefore not the most skewed data points in the sets. By contrast, if the model were applied based on a roughness equal to the sediment diameter (not shown in the figure), a mean underprediction by a factor of 1.9 would be obtained.

Figure 13 shows a comparison between bedload predictions of the analytical model and sediment transport measurements of purely asymmetric waves ($Sk = 0$) conducted in oscillating water tunnels (King 1991, steep front and steep rear wave series, $As = \pm 0.56$; Watanabe & Sato 2004, cases 1–33, $0.10 < As < 0.36$; van der A *et al.* 2010, coarse and medium sand series, $0.11 < As < 0.39$). King's runs are forward- and backward-leaning half waves, consisting of a forward stroke of the wavemaker. In contrast, Watanabe & Sato and van der A *et al.* simulated the complete oscillatory motion and measured the average transport rate over the entire wave cycle under forward-leaning waves. Again, our model's predictions are based on the wave velocities inferred from the motion of the wave piston. The predicted bed shear stresses are based on the total mobile-bed roughness. Only bedload-dominated cases, for which the predicted $u_{*m}/w_s < 4$, are shown in the figure. The predictions agree reasonably with the data (with a mean underprediction by a factor of 1.4), although there is disagreement with Watanabe and Sato's coarse-grain cases (cases 16–21, numbered in figure 13) and with King's steep rear cases (corresponding to offshore, i.e. negative, transport). The reliability of the former is dubious (see discussion by Gonzalez-Rodriguez & Madsen 2007), while the latter are within a factor of two difference with respect to the model's predictions. It is noted that the negative transport rates measured by King correspond to laboratory waves that are backward-leaning in shape, which is opposite to the shape of real asymmetric waves in the sea. Therefore, the positive and negative transport measurements by King all illustrate the same physical phenomenon, of asymmetric waves yielding a net transport in the forward-leaning direction. It is also noted that King's experiments correspond to half waves started from rest. The bed shear stresses under a half wave started from rest are smaller than those under steady-state conditions, and therefore our model's moderate overpredictions of King's transport rates are expected. We also recall that, unlike purely skewed Stokes second-order waves, application of the analytical model to asymmetric wave conditions generally involves the approximation of their

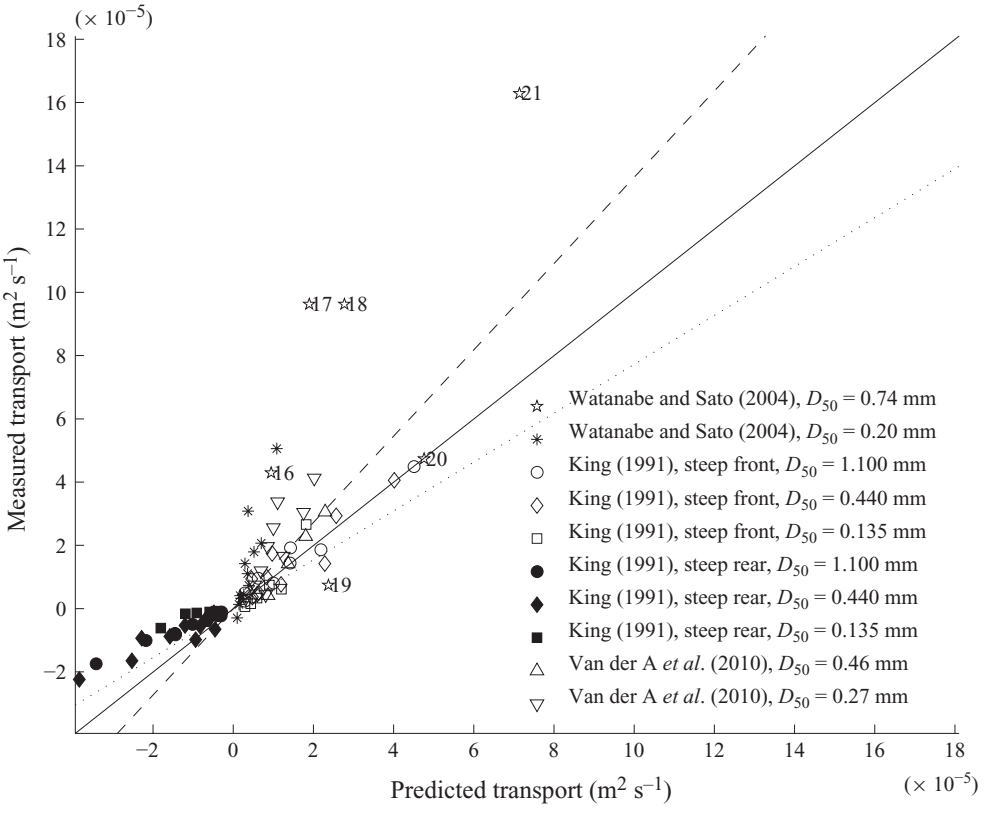

FIGURE 13. Comparison between measured and predicted average sediment transport rates under asymmetric, non-skewed waves for bedload-dominated cases ($u_{*m}/w_s < 4$). Predictions are obtained using the analytic boundary-layer model with mobile-bed roughness. The solid line corresponds to perfect agreement between predictions and measurements, while the dashed line is the least-squares fit to the data (underprediction by a factor of 1.4) and the dotted line is the least-squares fit to King's data only (overprediction by a factor of 1.3).

near-bed velocity time series by the two first Fourier harmonics, which will affect the accuracy of the transport rate predictions. By contrast, if the model were applied based on a roughness equal to the sediment diameter (not shown in the figure), a mean underprediction by a factor of 2.4 would be obtained. Van der A *et al.* (2010) compared the proficiency of different existing models in predicting their sediment transport data using the BSS quantifier. The closer the BSS to one, the better the predictions. The models considered by van der A *et al.* (2010) to predict their coarse-grain data (the one where bedload is dominant) yielded BSS values between −8.11 for (Hoefel & Elgar 2003) worst predictions and 0.69 for (Gonzalez-Rodriguez & Madsen 2007) best predictions. The present model performs better, yielding BSS = 0.80 for this dataset.

Figure 14 shows a comparison between predictions of the analytical model based on the mobile-bed roughness and the experimental data set of sinusoidal waves plus a current by Dohmen-Janssen *et al.* (2002, series E, I and J). Only bedload-dominated cases, for which the predicted $u_{*m}/w_s < 4$, are shown in each figure, where u_{*m} is now the maximum combined wave-current shear velocity. The predictions agree reasonably with the measurements, with a mean overprediction by a factor of 1.6; by contrast, if

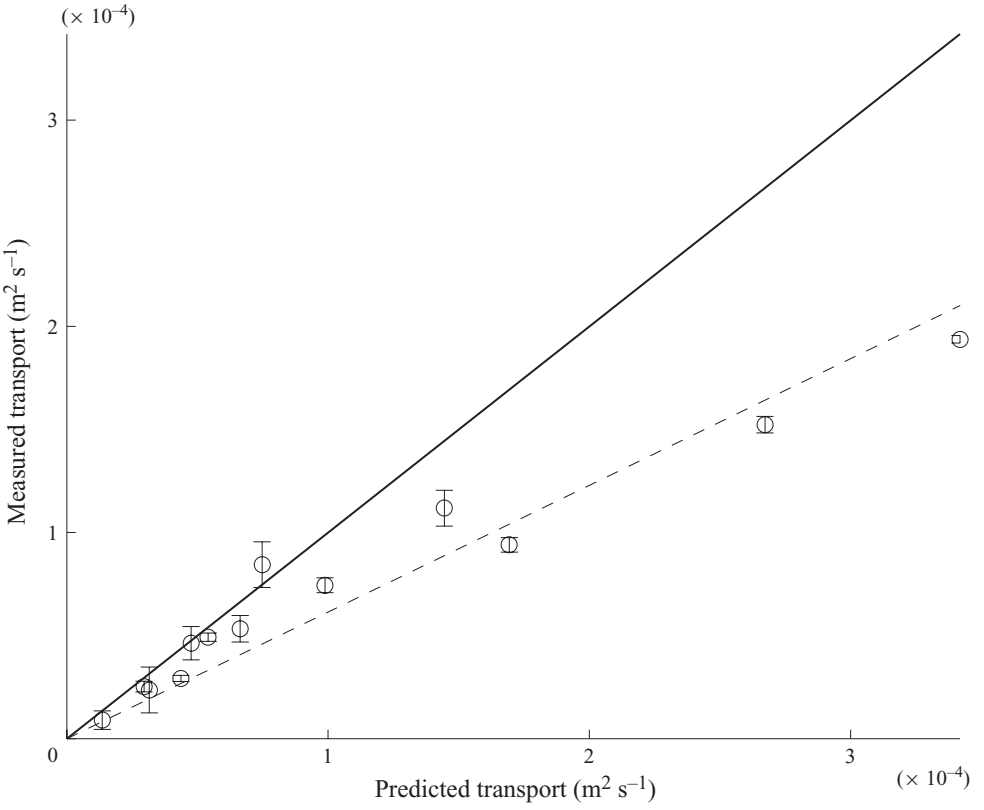

FIGURE 14. Comparison between measured Dohmen-Janssen *et al.* (2002) and predicted average sediment transport rates in current direction for co-directional sinusoidal waves and currents for bedload-dominated cases ($u_{*m}/w_s < 4$). Predictions are obtained using the analytic boundary-layer model with mobile-bed roughness. The solid line corresponds to perfect agreement between predictions and measurements, while the dashed line is the least-squares fit to the data and corresponds to an overprediction by a factor of 1.6.

a roughness equal to the sediment diameter were used, the model would yield a mean underprediction by a factor of 2.2 (not shown in the figure). The analytical model's predictions shown here use a wave boundary-layer thickness based on a 1 % departure from the free-stream velocity (see § 2.6). If instead the boundary-layer thickness were based on a 3 % departure from the free-stream velocity, good agreement between the analytical model's predictions and measurements would be obtained for all data in figure 14. This alternative boundary-layer thickness definition would, however, worsen the reasonable agreement with measured current velocity profiles discussed in § 4.3.

6. Conclusion

We present an analytical characterization of the turbulent boundary-layer flow in an oscillating water tunnel under an asymmetric and skewed wave (characterized by its two first Fourier harmonics) plus a weak current. Following the work of Trowbridge & Madsen (1984*a*, *b*), we account for the time dependence of the eddy viscosity. While Trowbridge and Madsen considered the general case of a propagating wave, we restrict

our analysis to a non-propagating wave in an oscillating water tunnel. Unlike the pure wave analysis of Trowbridge and Madsen, we account for an imposed collinear weak current. Also, while Trowbridge and Madsen assumed a bilinear structure of the eddy viscosity, we assume a more sophisticated vertical structure that accounts for the finite thickness of the wave boundary layer and for the effects of the (imposed or wave-induced) current turbulence. Our analysis yields closed-form analytical solutions for the flow field and the bed shear stresses in an oscillating water tunnel. Even in the absence of a current, we identify the existence of a mean flow (boundary-layer streaming) that arises from the interaction between the velocity and the time-varying eddy viscosity. An expression for the wave boundary-layer thickness as a function of the relative bottom roughness is also presented.

To complete the hydrodynamic characterization of the oscillating water tunnel, we account for the effect of the cross-sectional geometry and the prescribed cross-sectional flux. Corresponding to most oscillating water tunnels, we consider a cross-section that is tall and narrow, for which the midline flow is governed by the sidewall boundary layers. Accounting for the sidewall boundary-layer effect is thus crucial to correct prediction of the hydrodynamics near the bottom. We compare the hydrodynamic predictions of the model with measurements for sinusoidal waves, skewed waves and waves combined with a current. The comparison with the eddy viscosities inferred from sinusoidal wave measurements (Jonsson & Carlsen 1976) demonstrate that our assumption of a time-varying eddy viscosity is correct. The model correctly predicts the boundary-layer streaming measured for skewed waves (Ribberink & Al-Salem 1995), for which the interaction between velocity and eddy viscosity results in offshore streaming close to the boundary, which is balanced by an onshore mean flux further from the boundary. We also apply the hydrodynamic model to yield reasonably accurate predictions of the current profiles for cases of waves combined with a current reported by Dohmen-Janssen (1999).

The hydrodynamic model yields analytical expressions for the bed shear stresses, accurate to second order, for oscillating water tunnel conditions; these expressions are readily combined with a bedload formula (Madsen 1991) to predict bedload transport rates in oscillating water tunnels. Without the use of any fitting parameter, the model successfully predicts bedload transport rates measured in several experimental studies for skewed waves, asymmetric waves, and sinusoidal waves plus a current when the mobile-bed roughness is used. In contrast, a roughness equal to the sediment diameter systematically yields underpredictions. We thus conclude that the appropriate sheet flow roughness that parametrizes the effective bed shear stress (the bed shear stress component that is responsible for transport) is the total, mobile-bed roughness. While for rippled beds the effective shear stress is smaller than the total shear stress, with the difference being the form drag, for sheet flow conditions the effective and the total bed shear stresses and roughnesses coincide. This mobile-bed roughness can be evaluated using (4.6), the total hydraulic sheet-flow roughness formula proposed by Herrmann & Madsen (2007).

Hydrodynamic differences between oscillating water tunnels and real waves appear to have a non-negligible effect on sediment transport (Ribberink *et al.* 2008; Fuhrman *et al.* 2009; Holmedal & Myrhaug 2009) and they cannot be neglected in the validation of surf zone sediment transport models. A model that successfully predicts sediment transport rates in oscillating water tunnels cannot be directly applied to prediction of surf zone transport rates. Conversely, it is not obvious that a model that is developed based on the propagating wave hydrodynamics can be validated against oscillating water tunnel measurements. In this article we present an analytical model

that specifically describes the hydrodynamics of an oscillating water tunnel and successfully predicts the measured sediment transport rates. This success validates the applicability of the proposed analytical approach, which can be extended to predict sediment transport due to real near-shore waves.

The financial support of Singapore National Research Foundation through the Singapore-MIT Alliance for Research and Technology's (SMART) Center for Environmental Sensing and Modeling (CENSAM) is gratefully acknowledged. The authors thank Dr J. Ribberink and Dr D. van der A for providing detailed information about their experimental work.

REFERENCES

van der A, D. A., O'Donoghue, T., Davies, A. G. & Ribberink, J. S. 2008 Effects of acceleration skewness on rough bed oscillatory boundary layer flow. In *Proceedings of the 31st International Conference on Coastal Engineering*, pp. 1583–1595. World Scientific.

van der A, D. A., O'Donoghue, T. & Ribberink, J. S. 2010 Measurements of sheet flow transport in acceleration-skewed oscillatory flow and comparison with practical formulations. *Coastal Engng* **57**, 331–342.

Abramowitz, M. & Stegun, I. A. 1965 *Handbook of Mathematical Functions*. Dover.

Ahmed, A. S. M. & Sato, S. 2003 A sheetflow transport model for asymmetric oscillatory flows. Part I. Uniform grain size sediments. *Coast. Engng J.* **45** (3), 321–337.

Bosboom, J. & Klopman, G. 2000 Intra-wave sediment transport modeling. In *Proceedings of the 27th International Conference on Coastal Engineering*, pp. 2453–2466. ASCE.

Calantoni, J. & Puleo, J. A. 2006 Role of pressure gradients in sheet flow of coarse sediments under sawtooth waves. *J. Geophys. Res.* **111**, C01010.

Clauser, F. H. 1956 The turbulent boundary layer. *Adv. Appl. Mech.* **4**, 1–51.

Davies, A. G. & Li, Z. 1997 Modelling sediment transport beneath regular symmetrical and asymmetrical waves above a plane bed. *Cont. Shelf Res.* **17**, 555–582.

Dibajnia, M. & Watanabe, A. 1992 Sheet flow under nonlinear waves and currents. In *Proceedings of the 23rd International Conference on Coastal Engineering*, pp. 2015–2028. ASCE.

Dohmen-Janssen, C. M. 1999 Grain size influence on sediment transport in oscillatory sheet flow. Phase lags and mobile-bed effects. PhD thesis, Technical Univeristy of Delft, Delft, Netherlands.

Dohmen-Janssen, C. M., Hassan, W. N. & Ribberink, J. S. 2001 Mobile-bed effects in oscillatory sheet flow. *J. Geophys. Res.* **106** (C11), 27103–27115.

Dohmen-Janssen, C. M., Kroekenstoel, D. F., Hassan, W. N. & Ribberink, J. S. 2002 Phase lags in oscillatory sheet flow: experiments and bed load modelling. *Coast. Engng* **46** (1), 61–87.

Drake, T. G. & Calantoni, J. 2001 Discrete particle model for sheet flow sediment transport in the near-shore. *J. Geophys. Res.* **106** (C9), 19859–19868.

Elfrink, B., Hanes, D. M. & Ruessink, B. G. 2006 Parameterization and simulation of near bed orbital velocities under irregular waves in shallow water. *Coast. Engng* **53** (11), 915–927.

Foster, D. L., Guenther, R. A. & Holman, R. A. 1999 An analytical solution to the wave bottom boundary layer governing equation under arbitrary wave forcing. *Ocean Engng* **26**, 595–623.

Fuhrman, D. R., Fredsoe, J. & Sumer, B. M. 2009 Bed slope effects on turbulent wave boundary layers. Part 2. Comparison with skewness, asymmetry, and other effects. *J. Geophys. Res.* **114**, C03025.

Gonzalez-Rodriguez, D. 2009 Wave boundary layer hydrodynamics and cross-shore sediment transport in the surf zone. PhD thesis, Massachusetts Institute of Technology, Cambridge, MA.

Gonzalez-Rodriguez, D. & Madsen, O. S. 2007 Seabed shear stress and bedload transport due to asymmetric and skewed waves. *Coast. Engng* **54** (12), 914–929.

Gonzalez-Rodriguez, D. & Madsen, O. S. 2008 Bedload transport due to asymmetric and skewed waves plus a current. In *Proceedings of the 31st International Conference on Coastal Engineering*, pp. 1596–1605. World Scientific.

GRANT, W. D. & MADSEN, O. S. 1979 Combined wave and current interaction with a rough bottom. *J. Geophys. Res.* **84** (C4), 1797–1808.

HASSAN, W. N. & RIBBERINK, J. S. 2005 Transport processes of uniform and mixed sands in oscillatory sheet flow. *Coast. Engng* **52** (9), 745–770.

HENDERSON, S. M., ALLEN, J. S. & NEWBERGER, P. A. 2004 Near-shore sandbar migration predicted by an eddy-diffusive boundary layer model. *J. Geophys. Res.* **109**, C06024.

HERRMANN, M. J. & MADSEN, O. S. 2007 Effect of stratification due to suspended sand on velocity and concentration distribution in unidirectional flows. *J. Geophys. Res.* **112**, C02006.

HOEFEL, F. & ELGAR, S. 2003 Wave-induced sediment transport and sandbar migration. *Science* **299**, 1885–1887.

HOLMEDAL, L. E. & MYRHAUG, D. 2006 Boundary layer flow and net sediment transport beneath asymmetrical waves. *Cont. Shelf Res.* **26**, 252–268.

HOLMEDAL, L. E. & MYRHAUG, D. 2009 Wave-induced steady streaming, mass transport and net sediment transport in rough turbulent ocean bottom boundary layers. *Cont. Shelf Res.* **29**, 911–926.

HSU, T.-J., ELGAR, S. & GUZA, R. T. 2006 Wave-induced sediment transport and onshore sandbar migration. *Coast. Engng* **53** (10), 817–824.

HSU, T.-J. & HANES, D. M. 2004 Effects of wave shape on sheet flow sediment transport. *J. Geophys. Res.* **109**, C05025.

JIMENEZ, J. A. & MADSEN, O. S. 2003 A simple formula to estimate settling velocity of natural sediments. *J. Waterw. Port Coast. Ocean Engng* **129** (2), 70–78.

JONSSON, I. G. & CARLSEN, N. A. 1976 Experimental and theoretical investigations in an oscillatory turbulent boundary layer. *J. Hydraul. Res.* **46**, 75–123.

KING, D. B. 1991 Studies in oscillatory flow bedload sediment transport. PhD thesis, University of California, San Diego.

LIU, H. & SATO, S. 2006 A two-phase flow model for asymmetric sheetflow conditions. *Coast. Engng* **53** (10), 825–843.

LONGUET-HIGGINS, M. S. 1953 Mass transport in water waves. *Phil. Trans. R. Soc. Lond.* A **245**, 535–581.

MADSEN, O. S. 1991 Mechanics of cohesionless sediment transport in coastal waters. In *Proceedings of Coastal Sediments '91*, pp. 15–27. ASCE.

MADSEN, O. S. 2002 Sediment transport outside the surf zone. In *Coastal Engineering Manual* (ed. T. Walton), pp. III-6-1–III-6-69. US Army Corps of Engineers.

MADSEN, O. S. & GRANT, W. D. 1976 Quantitative description of sediment transport by waves. In *Proceedings of the 15th International Conference on Coastal Engineering*, pp. 1093–1112. ASCE.

NIELSEN, P. 2006 Sheet flow sediment transport under waves with acceleration skewness and boundary layer streaming. *Coast. Engng* **53** (9), 749–758.

O'DONOGHUE, T. & WRIGHT, S. 2004 Flow tunnel measurements of velocities and sand flux in oscillatory sheet flow for well-sorted and graded sands. *Coast. Engng* **51** (11–12), 1163–1184.

RIBBERINK, J. S. 1998 Bed-load transport for steady flows and unsteady oscillatory flows. *Coast. Engng* **34** (1–2), 59–82.

RIBBERINK, J. S. & AL-SALEM, A. A. 1994 Sediment transport in oscillatory boundary layers in cases of rippled beds and sheet flow. *J. Geophys. Res.* **99** (C6), 12707–12727.

RIBBERINK, J. S. & AL-SALEM, A. A. 1995 Sheet flow and suspension of sand in oscillatory boundary layers. *Coast. Engng* **25** (3–4), 205–225.

RIBBERINK, J. S., VAN DER WERF, J. J., O'DONOGHUE, T. & HASSAN, W. N. M. 2008 Sand motion induced by oscillating flows: sheet flow and vortex ripples. *J. Turbul.* **9**, 1–32.

VAN RIJN, L. C., WALSTRA, D. J. R., GRASMEIJER, B., SUTHERLAND, J., PAN, S. & SIERRA, J. P. 2003 The predictability of cross-shore bed evolution of sandy beaches at the time scale of storms and seasons using process-based profile models. *Coastal Engng* **47**, 295–327.

RUESSINK, B. G., VAN DEN BERG, T. J. J. & VAN RIJN, L. C. 2009 Modeling sediment transport beneath skewed asymmetric waves above a plane bed. *J. Geophys. Res.* **114**, C11021.

SILVA, P. A., TEMPERVILLE, A. & SANTOS, F. S. 2006 Sand transport under combined current and wave conditions: a semi-unsteady, practical model. *Coast. Engng* **53**, 897–913.

Suntoyo, Tanaka, H. & Sana, A. 2008 Characteristics of turbulent boundary layers over a rough bed under saw-tooth waves and its application to sediment transport. *Coast. Engng* **55**, 1102–1112.

Trowbridge, J. 1983 Wave-induced turbulent flow near a rough bed: implications of a time-varying eddy viscosity. PhD thesis, Massachusetts Institute of Technology, Cambridge, MA.

Trowbridge, J. & Madsen, O. S. 1984*a* Turbulent wave boundary layers. Part 1. Model formulation and first-order solution. *J. Geophys. Res.* **89** (C5), 7989–7997.

Trowbridge, J. & Madsen, O. S. 1984*b* Turbulent wave boundary layers. Part 2. Second-order theory and mass transport. *J. Geophys. Res.* **89** (C5), 7999–8007.

Watanabe, A. & Sato, S. 2004 A sheet-flow transport rate formula for asymmetric, forward-leaning waves and currents. In *Proceedings of the 29th International Conference on Coastal Engineering*, pp. 1703–1714. World Scientific.

van der Werf, J. J., Schretlen, J. J. L. M., Ribberink, J. S. & O'Donoghue, T. 2009 Database of full-scale laboratory experiments on wave-driven sand transport processes. *Coast. Engng* **56** (7), 726–732.

Yu, X., Hsu, T.-J. & Hanes, D. M. 2010 Sediment transport under wave groups: relative importance between nonlinear waveshape and nonlinear boundary layer streaming. *J. Geophys. Res.* **115**, C02013.